STRUCTURE AND EVOLUTION OF DEBRIS DISKS AROUND F-TYPE STARS. I. OBSERVATIONS, DATABASE, AND BASIC EVOLUTIONARY ASPECTS

A. Moór[1], I. Pascucci[2], Á. Kóspál[3], P. Ábrahám[1], T. Csengeri[4], L. L. Kiss[1,5], D. Apai[2], C. Grady[6,7], Th. Henning[8], Cs. Kiss[1], D. Bayliss[9], A. Juhász[8], J. Kovács[10], AND T. Szalai[11]

[1] Konkoly Observatory of the Hungarian Academy of Sciences, P.O. Box 67, H-1525 Budapest, Hungary; moor@konkoly.hu
[2] Space Telescope Science Institute, 3700 San Martin Drive, Baltimore, MD 21218, USA
[3] Leiden Observatory, Leiden University, Niels Bohrweg 2, NL-2333 CA Leiden, The Netherlands
[4] Laboratoire AIM, CEA/DSM, IRFU/Service d'Astrophysique, 91191 Gif-sur-Yvette Cedex, France
[5] Sydney Institute for Astronomy, School of Physics A28, University of Sydney, NSW 2006, Australia
[6] NASA Goddard Space Flight Center, Code 667, Greenbelt, MD 20771, USA
[7] Eureka Scientific, 2452 Delmer Street, Suite 100, Oakland, CA 94602, USA
[8] Max-Planck-Institut für Astronomie, Königstuhl 17, 69117 Heidelberg, Germany
[9] Research School of Astronomy and Astrophysics, The Australian National University, Mount Stromlo Observatory, Cotter Road, Weston Creek, ACT 2611, Australia
[10] Gothard Astrophysical Observatory, ELTE University, 9707 Szombathely, Hungary
[11] Department of Optics and Quantum Electronics, University of Szeged, 6720 Szeged, Dóm tér 9, Hungary

ABSTRACT

Although photometric and spectroscopic surveys with the *Spitzer Space Telescope* remarkably increased the number of well-studied debris disks around A-type and Sun-like stars, detailed analyses of debris disks around F-type stars remained less frequent. Using the MIPS camera and the Infrared Spectrograph (IRS) spectrograph, we searched for debris dust around 82 F-type stars with *Spitzer*. We found 27 stars that harbor debris disks, nine of which are new discoveries. The dust distribution around two of our stars, HD 50571 and HD 170773, was found to be marginally extended on the 70 μm MIPS images. Combining the MIPS and IRS measurements with additional infrared and submillimeter data, we achieved excellent spectral coverage for most of our debris systems. We have modeled the excess emission of 22 debris disks using a single temperature dust ring model and of five debris systems with two-temperature models. The latter systems may contain two dust rings around the star. In accordance with the expected trends, the fractional luminosity of the disks declines with time, exhibiting a decay rate consistent with the range of model predictions. We found the distribution of radial dust distances as a function of age to be consistent with the predictions of both the self-stirred and the planetary-stirred disk evolution models. A more comprehensive investigation of the evolution of debris disks around F-type stars, partly based on the presented data set, will be the subject of an upcoming paper.

Key words: circumstellar matter – infrared: stars

Online-only material: color figure

1. INTRODUCTION

Nearly all young stars harbor circumstellar disks, which initially serve as reservoirs for mass accretion and later can become the birthplaces of planetary systems. During this latter process, the originally submicron-sized dust grains start growing, and their aggregation is believed to lead to km-sized planetesimals (for a review, see Apai & Lauretta 2010, and references therein). Non-destructive collisions between planetesimals result in the formation of subsequently larger bodies. These events happen first in the inner disk due to the shorter collisional timescales, then the process propagates outward (Kenyon & Bromley 2004a). The newly formed Pluto-sized protoplanets stir up the motion of leftover smaller bodies in their vicinity, initializing a collisional cascade. As they become more energetic, collisions result in the erosion of planetesimals and the production of small dust grains. An optically thin *debris disk* is formed, in which the second-generation, short-lived dust grains are continuously replenished by collisions and/or evaporation of planetesimals (Backman & Paresce 1993; Wyatt 2008). This *self-stirring* mechanism is not the sole feasible way to incite destructive collisions between minor bodies. Giant planets, formed previously in the primordial disk, or stellar companions can also dynamically excite the motion of planetesimals via their secular

perturbation, even at a significant distance from the planetesimal disk. Thus, these large bodies can also initiate and govern the formation and evolution of a debris disk (Mustill & Wyatt 2009), providing an alternative stirring mechanism. In a debris disk, mutual collisions grind down planetesimals to small dust grains that are then ejected by radiation pressure, or in more tenuous disks removed by the Poynting–Robertson (PR) drag (Dominik & Decin 2003; Wyatt 2005). This process is accompanied by the depletion of the reservoir planetesimal belt and eventually leads to the decline of the debris production (Wyatt et al. 2007a; Löhne et al. 2008).

Due to the strong link between the debris dust and the unseen planetesimals, the investigations of the smallest particles of debris systems can lead to a better understanding of the formation and evolution of planetesimal belts and, eventually, the formation and evolution of planetary systems. The observational verification of the different aspects of planetesimal formation and evolutionary model predictions requires a detailed study of the incidence of stars with infrared (IR) emission due to debris dust and investigating the change of debris disk properties (e.g., radius of the dust ring and fractional luminosity) with age. The ideal way would be to resolve and observe many debris disks in scattered light or in thermal emission from optical to millimeter wavelengths with good wavelength coverage. In reality,

however, the number of resolved disks is very limited and the spectral energy distribution (SED) of the dust emission was measured for most debris systems only in a few infrared bands. The fundamental parameters of the disks have to be estimated from these sparsely sampled SEDs. The interpretation of SEDs is ambiguous (e.g., considering the radial location of the dust) but by handling a debris disk sample as an ensemble, one can obtain a meaningful picture about the basic characteristics of the parent planetesimal belt(s) and about the evolutionary trends.

The current theoretical models dealing with the buildup of planetesimals (Kenyon & Bromley 2004a, 2008) and with the steady-state collisional evolution of the planetesimal belts (Dominik & Decin 2003; Wyatt et al. 2007a; Löhne et al. 2008) predict how the fundamental properties of debris disks evolve with time. At a specific radius, the peak of the dust emission is believed to coincide with the formation of 1000–2000 km sized planetesimals. After this stage—parallel with the depletion of planetesimals—the dust emission decreases with time. The evolution of the disk can be traced both in the variation of incidence of disks with time and in the evolution of the brightness of dust emission. The different models predict that the dust fractional luminosity, the ratio of the energy radiated by the dust to the stellar luminosity, varies with time as t^{-n}, where $n = 0.3$–1 in disks where collisions are the dominant removal process (Dominik & Decin 2003; Wyatt et al. 2007a; Löhne et al. 2008; Kenyon & Bromley 2008). The unique sensitivity of the *Spitzer Space Telescope* in the MIPS 24 μm band allowed the detection of stellar photospheres and a small amount of excess for a large number of field stars (e.g., Rieke et al. 2005; Meyer et al. 2008) and even for relatively distant open cluster members (e.g., Young et al. 2004; Gorlova et al. 2006; Siegler et al. 2007; Currie et al. 2008; Balog et al. 2009). The latter observations enabled the study of the evolution of warm dust around well-dated sample stars. Investigating early (late B- and A-) type stars Rieke et al. (2005) demonstrated a decline of debris disks with age: older stars show excess emission less frequently and with lower fractional excess than the younger ones. Siegler et al. (2007) found similar evolutionary trends for debris disks encircling later type stars (F, G, K). Based on observations of more than 300 Sun-like stars with spectral type of F5–K3, Meyer et al. (2008) argued that the 24 μm excess fraction for this sample is roughly constant for ages ≲300 Myr and declines thereafter (see also in Carpenter et al. 2009b). Recently, Gáspár et al. (2009) and Carpenter et al. (2009a) gave a summary of the evolution of 24 μm excesses around B7–K5-type stars. Confirming the previous results they concluded that both the incidence of 24 μm excess and the excess luminosity monotonically decrease with time at ages ≳20 Myr. Utilizing the observations of different infrared space missions (*IRAS*, the *Infrared Space Observatory* (*ISO*), *Spitzer*), the predicted evolutionary trend in the fractional luminosities was also established (Decin et al. 2003; Su et al. 2006; Wyatt et al. 2007b; Rhee et al. 2007; Carpenter et al. 2009b). In an extended planetesimal disk both the stirring by Pluto-sized planetesimals that were born in the same belt and the dynamical excitation by secular perturbation of distinct giant planets are thought to be accompanied by the outward propagation of the dust production site with time (Kenyon & Bromley 2008; Mustill & Wyatt 2009). The observational evidence for such a delayed initiation of the collisional cascade as the function of radial location is not yet conclusive. Some surveys did not report any trend in the evolution of the radius with age (e.g., Najita & Williams 2005), while studying debris disks around B- and A-type stars Rhee et al. (2007) found some evidence that the radius of dust belts is increasing with stellar age.

Thanks to the recent photometric and spectroscopic surveys with the *Spitzer Space Telescope*, the number of debris disks with detailed SED at mid- and far-IR wavelengths has been increased significantly (Chen et al. 2006; Rieke et al. 2005; Su et al. 2006; Carpenter et al. 2008; Rebull et al. 2008; Trilling et al. 2008). This improvement is especially remarkable for disks around A-type and Sun-like stars (late F-, G-, and K-type stars). The comparison of these data with the predictions of quasi-steady-state evolutionary models showed that most observed trends for A-type and Sun-like stars can be reproduced adequately (Wyatt 2008; Carpenter et al. 2009b). Kennedy & Wyatt (2010) confronted the *Spitzer* observations of A-type stars with an analytic model that also take into account the effects of the self-stirring on the disk evolution. Utilizing this model they were able to reproduce the observed trends and they obtained rough estimates for some initial parameters (e.g., average mass) of disks around A-type stars. It was also concluded that debris disks are narrow belts rather than extended disks. According to the models, F-type stars are expected to be an intermediate type between the A-type and Sun-like stars in terms of debris disk evolution as well: (1) their disks are predicted to evolve faster than those around main-sequence stars of later types (in disks with identical surface density distribution, the timescale of planetesimal formation processes are thought to be proportional to $M_*^{-1/2}$) and (2) F-type stars live much longer than A-type stars (the main-sequence lifetime of a 1.4 $M_\odot$ F5-type star is three times longer than the main-sequence lifetime of a 2.0 $M_\odot$ A5-type star), making it possible to follow disk evolution for a significantly longer time. Up to now the number of detailed studies of debris disks around F-type stars is modest compared to the A-type and Sun-like samples, preventing us from understanding the evolutionary aspects.

In this paper, we present the results of a large survey with the *Spitzer Space Telescope* that focuses on debris disks around F-type stars. Our main goals are to (1) significantly increase the number of debris disks with detailed SED around F-type stars, (2) investigate the variations of fundamental properties of the disks and compare the observed trends with the predicted ones, and (3) compare the evolutionary trends obtained for disks around A-, F-, and G/K-type stars. In the present paper, we review the target selection (Section 2), observations and data reduction aspects of the F-stars program (Section 3). We identify stars with infrared excess, model their SED and estimate the fundamental properties of the observed debris disks (Section 4). Using the derived parameters we investigate the diversity of the fundamental disk properties and compare the observed trends with the predictions (Section 5).

Four new warm disks—discovered in the framework of this program—have already been analyzed and published (Moór et al. 2009). The evolutionary aspects of the current data set—supplemented by the recently discovered four warm debris systems as well as additional debris disks around F-type stars observed by *Spitzer* from the literature—will be further analyzed in an upcoming paper (A. Moór et al. 2011a, in preparation).

2. SAMPLE SELECTION

Our primary intention was to study the variations of the disk properties, thus in the sample selection we focused on stars where previous IR observations hinted on the existence of excess emission. Although the formation of planetesimals may last as

much as hundred million years in an extended disk, the most active period of this process is restricted to the first few tens of millions years (Kenyon & Bromley 2008). The possible outward propagation of the planetesimal formation can be verified in this period. Since the age of nearby moving groups overlaps well with this period, they are favorable, nearby, and well-dated places for investigations of the debris disk evolution process. Thus, the above-mentioned sample was supplemented by several F-type members of the nearby young kinematic groups. For these young stars we did not require *a priori* information about the presence of emission in excess to the stellar photosphere. Because of the selection method, the sample is inherently biased with respect to the presence of disks, therefore it cannot be used to study the incidence of debris disks around F-type stars.

With the aim of constructing a list of F-type main-sequence (and some subgiant) stars, where earlier observations indicated the presence of mid- and/or far-infrared excesses, we carried out a systematic search using the data of the *IRAS* and *ISO* satellites. For the selection of *IRAS*-based candidates, we collected all sources from the *IRAS* Faint Source Survey Catalogue (*IRAS* FSC; Moshir et al. 1989) and the *IRAS* Serendipitous Survey Catalogue (*IRAS* SSC; Kleinmann et al. 1986) having at least moderate flux quality at 25 and 60 μm. The positions of the *IRAS* sources were cross-correlated with the entries of the *Hipparcos* Catalogue (ESA 1997) and the *Tycho-2* Spectral Type Catalog (Wright et al. 2003), and we selected only those objects where the positional match was within 30''. Giant stars were omitted from the sample on the basis of the spectral information or the absolute magnitude. For the identification of stars with excess we used the method of Mannings & Barlow (1998). First, we computed the ratios of measured 25 μm and 60 μm flux densities to the measured flux at 12 μm ($R_{12/25} = \frac{F_{12}}{F_{25}}$, $R_{12/60} = \frac{F_{12}}{F_{60}}$) as well as the error of the ratios ($\delta R_{12/25} = \frac{F_{12}}{F_{25}}\sqrt{(\frac{\delta F_{12}}{F_{12}})^2 + (\frac{\delta F_{25}}{F_{25}})^2}$, $\delta R_{12/60} = \frac{F_{12}}{F_{60}}\sqrt{(\frac{\delta F_{12}}{F_{12}})^2 + (\frac{\delta F_{60}}{F_{60}})^2}$). Then, applying a Kurucz model atmosphere of a typical F-type star (a model with effective temperature of 6500 K, $\log g = 4.25$, solar metallicity), we derived the expected photospheric flux ratios for the specific *IRAS* bands ($R^*_{12/25}$, $R^*_{12/60}$). We calculated the significance of the differences between the observed and expected ratios as $S_{12/25} = \frac{R_{12/25} - R^*_{12/25}}{\delta R_{12/25}}$ and $S_{12/60} = \frac{R_{12/60} - R^*_{12/60}}{\delta R_{12/60}}$. Finally, we selected those objects where $S_{12/25} < -2.5$ or/and $S_{12/60} < -3.0$. Due to the low spatial resolution of *IRAS*, many of the positional coincidences between a star and an infrared source could be false (Moór et al. 2006; Rhee et al. 2007). In order to reject objects that are possibly affected by source confusion, we applied the same criteria as those adopted in Section 2.3 in Moór et al. (2006).

Observations with *ISO* confirmed the existence of IR excess and the positional agreement between the optical and IR source for several of our *IRAS*-based candidates. Moreover, the compiled list was further supplemented by five *ISO*-based discoveries (Spangler et al. 2001; Decin et al. 2003).

The list of F-type stars belonging to different nearby young stellar kinematic groups (e.g., Tucana-Horologium association and AB Dor moving group) was adopted from the catalog of Zuckerman & Song (2004b). This initial list was amended by adding several new unpublished moving group members (A. Moór et al. 2011b, in preparation).

After merging the lists, we excluded all those objects that were reserved by other *Spitzer* programs. Among the finally selected 82 candidates, 27 were based on hints for excess emission

at 25 μm (Warm Disk Candidates, hereafter WDCs), 46 are suspected to exhibit IR excess at longer wavelengths (Cold Disk Candidates, hereafter CDCs), and 9 were selected because of their kinematic group membership (Moving Group Members, hereafter MGMs). Note that many stars selected on the basis of their suspected excess are also young kinematic group members. The basic properties of the sample stars as well as the reason for their selection are listed in Table 1.

2.1. Basic Properties of the Selected Objects

In order to estimate some basic properties of our stars and to provide photospheric flux predictions at relevant mid- and far-IR wavelengths, we modeled the stellar photosphere by fitting an ATLAS9 atmosphere model (Castelli & Kurucz 2003) to the optical and near-IR observations (*Hipparcos*, *Tycho-2*, 2MASS). The surface gravity value was fixed during the fitting procedure. If there was no indication that a star has already left the main-sequence—based on its position in the H-R diagram and/or spectroscopic information—we adopted a value of $\log g = 4.25$ corresponding to the main-sequence stage. For evolved objects the $\log g$ values were either taken from literature or computed from available data (see Table 1 for details). The metallicity data were also collected from the literature. In the cases where more than one [Fe/H] estimates were available for a star, we used the average. If no metallicity information was found for a specific star, we adopted solar metallicity. Most of our stars are located inside the Local Bubble, where the mean extinction is low (Lallement et al. 2003). Thus, for stars within 80 pc the visual extinction was neglected (A_V set to 0.0). For more distant objects and for stars without reliable distance information, the A_V value was a free parameter in fitting the photosphere. Our sample contains 23 multiple systems (see Table 1). For close binary systems with separation <5'', we used the combined photometry of the components, except for HD 122510 and HD 199391, where good quality photometric data were available separately for each component. In the latter cases the fitting was performed for the different components separately and then the obtained photospheric models were co-added. The fixed ($\log g$, [Fe/H]) and fitted ($T_{\rm eff}$, A_V) parameters are quoted in Table 1.

3. OBSERVATIONS AND DATA REDUCTION

We performed observations using the Multiband Imaging Photometer for *Spitzer* (MIPS; Rieke et al. 2004) and the Infrared Spectrograph (IRS; Houck et al. 2004) on the *Spitzer Space Telescope* (Werner et al. 2004) in the framework of the programs PID: 3401, 20707, and 40566 (PI: P. Ábrahám). The MIPS photometry of HD 35114 was taken from the *Spitzer* Archive (PID: 3600, PI: I. Song). The MIPS images were obtained in photometric imaging mode (default scale, small-field size). All of our objects were measured at 24 μm and 70 μm, CDCs and most MGMs (in total 52 objects) were observed at 160 μm as well. In the 24 μm band we performed two observation cycles with integration time of 3 s, typically providing 28 Data Collection Event frames per source. At 70 μm and 160 μm 2–10 cycles were made, the integration time was set to 3 s or 10 s depending on the actual source. We obtained low-resolution spectra, using standard IRS staring mode observations with the Short–Low and Long–Low modules, which are sufficient to outline the continuum and the broad spectral features. Whenever it was possible, peak-up observations in high accuracy IRS or PCRS mode were used to

Table 1
Basic Properties of our Target List

ID	SpT	V (mag)	D (pc)	[Fe/H]	Ref.	$\log g$	$T_{\rm eff}$ (K)	A_V (mag)	Mult.	Sep. ($''$)	Ref.	Sel. cr.
(1)	(2)	(3)	(4)	(5)	(6)	(7)	(8)	(9)	(10)	(11)	(12)	(13)
HD 3670	F5V	8.23	(76.0)	−0.13	1	4.25	6480	0.00	N	. . .	. . .	2
HD 14691	F0V	5.43	29.7	−0.12	1, 2	4.25	6800	0.00	N	. . .	. . .	1
HD 15060	F5V	7.02	76.0	−0.14	1	4.00	6260	0.00	N	. . .	. . .	1
HD 15115	F2	6.79	45.2	−0.06	1	4.25	6780	0.00	N	. . .	. . .	1
HD 15745	F0	7.47	63.5	−0.10	1	4.25	6860	0.00	N	. . .	. . .	1
HD 16743	F0/F2III/IV	6.78	58.9	−0.13	1	4.25	7000	0.00	Y	216.2	1	1
HD 17390	F3IV/V	6.48	48.0	0.03	1	4.25	6840	0.00	N	. . .	. . .	1
BD+49° 896	F4V	9.68	(175.0)	−0.15	3	4.25	6740	0.06	N	. . .	. . .	1
HD 20759	F5V	7.70	76.8	−0.48	1	4.00	6280	0.00	N	. . .	. . .	1
HD 24636	F3IV/V	7.13	54.1	−0.11	1	4.25	6820	0.00	N	. . .	. . .	2
HD 25570	F2V	5.45	34.9	−0.29	1	4.00	6760	0.00	N	. . .	. . .	1
HD 25953	F5	7.83	55.2	−0.22	1	4.25	6240	0.00	N	. . .	. . .	2
HD 27429	F3:V...	6.11	48.3	0.01	1	4.00	6720	0.00	Y	. . .	2	1
HD 30447	F3V	7.85	80.3	−0.21	1	4.25	6800	0.00	N	. . .	. . .	1, 2
HD 32195	F7V	8.14	61.0	−0.13	1	4.25	6180	0.00	N	. . .	. . .	2
HD 30743	F3/F5V	6.27	33.8	−0.38	1, 2, 4, 5	4.25	6440	0.00	N	. . .	. . .	1
HD 33081	F7V	7.04	50.6	−0.19	1	4.25	6360	0.00	N	. . .	. . .	1
HD 33276	F2IV	4.81	165.0	0.27	6, 7	3.25	6920	0.00	Y	0.300	3	1
HD 34739	F7IV/V	9.33	(121.0)	. . .	. . .	4.25	6280	0.00	N	. . .	. . .	1
HD 35114	F6V	7.39	48.3	−0.18	1	4.25	6200	0.00	N	. . .	. . .	2
HD 35841	F5V	8.91	(96.0)	. . .	. . .	4.25	6460	0.00	N	. . .	. . .	1, 2
HD 36248	F8	8.05	73.6	0.11	1	4.25	5960	0.06	Y	3.800	3	1
HD 36968	F2V	9.02	(140.0)	. . .	. . .	4.25	6880	0.00	N	. . .	. . .	1, 2
HD 37402	F6V	8.38	78.2	−0.15	1	4.25	6160	0.00	N	. . .	. . .	2
HD 38905	F6/F7V	9.73	(140.0)	. . .	. . .	4.25	6240	0.04	N	. . .	. . .	1
HD 47412	F2	6.82	111.0	−0.03	1	4.00	6300	0.00	Y	0.500	3	1
HD 48391	F5	7.89	58.3	−0.20	1	4.25	6160	0.00	N	. . .	. . .	2
HD 50571	F7III-IV	6.11	33.6	−0.02	1, 2	4.25	6480	0.00	N	. . .	. . .	1
HD 55003	F2	7.04	60.1	−0.02	1	4.00	6340	0.00	Y	. . .	2	1
HD 56099	F8	7.62	86.7	−0.03	1	4.00	6060	0.00	Y	0.130	4	1
HD 58853	F5V	9.07	122.4	. . .	. . .	4.25	6280	0.00	N	. . .	. . .	1
HD 61518	F5V	7.88	62.0	−0.19	1	4.25	6340	0.00	N	. . .	. . .	2
HD 67587	F8	6.65	46.8	−0.19	1	4.00	5980	0.00	Y	. . .	2	1
HD 69351	F8	7.16	80.0	0.08	1	4.00	5980	0.00	Y	1.400	3	1
HD 79873	F5	6.73	68.3	0.13	1	4.00	6400	0.00	Y	2.100	3	1
HD 82821	F8	8.69	74.7	. . .	. . .	4.25	6140	0.00	Y	. . .	2	1
HD 86146	F6Vs	5.11	28.1	0.02	1	4.00	6360	0.00	Y	. . .	5	1
PPM 7774	F5	8.96	(116.0)	. . .	. . .	4.25	6520	0.00	N	. . .	. . .	1
HD 103257	F2V	6.62	63.4	−0.39	1	4.00	6980	0.00	N	. . .	. . .	1
HD 107067	F8...	8.69	66.0	−0.09	1, 8, 9	4.25	6060	0.00	N	. . .	. . .	1
HD 108102	F8...	8.12	95.1	−0.13	1	4.00	6060	0.00	N	. . .	. . .	1
HD 113337	F6V	6.01	36.9	0.06	1, 10	4.25	6600	0.00	Y	119.7	3	1
HD 114905	F7V	6.83	61.4	−0.21	1	4.00	6280	0.00	N	. . .	. . .	1
HD 117360	F6V	6.52	35.2	−0.34	1, 2	4.25	6400	0.00	Y	22.40	3	1
HD 120160	F0IV/V	7.67	138.3	0.02	1	3.75	6760	0.00	N	. . .	. . .	1
HD 122106	F8V	6.36	77.5	0.08	1, 11	3.75	6280	0.00	N	. . .	. . .	1
HD 122510	F6V	6.18	38.2	−0.11	1, 2	4.25	6600	0.00	Y	1.900	3	1
HD 124988	F0	6.88	96.0	−0.09	1	4.00	6880	0.00	N	. . .	. . .	1
HD 125451	F5IV	5.41	26.1	−0.00	1, 12	4.25	6660	0.00	N	. . .	. . .	1
HD 127821	F4IV	6.10	31.8	−0.18	1	4.25	6660	0.00	N	. . .	. . .	1
HD 131495	F2	6.87	72.3	−0.13	1	4.00	6460	0.00	N	. . .	. . .	1
HD 134150	F8	9.84	(166.0)	. . .	. . .	4.25	6460	0.03	N	. . .	. . .	1
HD 136580	F5	6.90	41.0	−0.15	1, 13	4.25	6180	0.00	Y	. . .	2	1
HD 136407	F2V	6.14	56.7	−0.08	1	4.00	6640	0.00	Y	44.40	3	1
HD 138100	F0	6.69	57.8	−0.07	1	4.00	6720	0.00	Y	. . .	2	1
HD 139798	F2V	5.76	35.7	−0.22	1, 12	4.00	6700	0.00	Y	. . .	2	1
HD 143840	F1V	8.11	132.3	−0.03	1	4.00	6680	0.47	N	. . .	. . .	1
HD 145371	G0	9.46	(144.0)	. . .	. . .	4.25	6480	0.00	N	. . .	. . .	1
HD 151044	F8V	6.48	29.3	−0.02	1, 9, 12, 13, 14, 15	4.25	6060	0.00	N	. . .	. . .	1
HD 153377	F2	7.55	64.0	−0.16	1	4.25	6620	0.00	N	. . .	. . .	1
HD 155990	F8	8.07	57.7	−0.18	1	4.25	6100	0.00	N	. . .	. . .	2
HD 156635	F8	6.66	40.3	−0.09	1, 16	4.25	6160	0.00	Y	. . .	2	1
HD 170773	F5V	6.22	37.0	−0.05	1, 2	4.25	6640	0.00	N	. . .	. . .	1
HD 184169	F2	8.20	(83.0)	. . .	. . .	4.25	6540	0.00	N	. . .	. . .	1

Table 1
(Continued)

ID	SpT	V (mag)	D (pc)	[Fe/H]	Ref.	$\log g$	$T_{\rm eff}$ (K)	A_V (mag)	Mult.	Sep. ($''$)	Ref.	Sel. cr.
(1)	(2)	(3)	(4)	(5)	(6)	(7)	(8)	(9)	(10)	(11)	(12)	(13)
HD 183577	F6V	6.48	41.6	−0.24	1	4.00	6100	0.00	Y	. . .	2	1
HD 185053	F5/F6V	8.83	(67.0)	. . .	. . .	4.25	5960	0.24	N	. . .	. . .	1
HD 189207	F2	8.08	116.3	−0.06	1	4.00	6780	0.00	N	. . .	. . .	1
HD 192486	F2V	6.55	44.7	−0.18	1	4.25	6820	0.00	N	. . .	. . .	1
HD 192758	F0V	7.03	(62.0)	−0.06	17	4.25	7080	0.00	N	. . .	. . .	1
HD 195952	F3V	8.12	153.4	−0.06	1	3.75	6240	0.06	N	. . .	. . .	1
HD 199391	F0/F2IV	7.12	78.7	. . .	. . .	4.00	7160	0.00	Y	4.800	3	1
PPM 171537	F8	9.23	(90.0)	. . .	. . .	4.25	5960	0.00	N	. . .	. . .	1
HD 204942	F7V	8.23	84.9	−0.14	1	4.25	6220	0.00	N	. . .	. . .	1
HD 205674	F3/F5IV	7.19	51.8	−0.23	1	4.25	6780	0.00	N	. . .	. . .	1
HD 206554	F5	7.12	65.9	−0.23	1	4.00	6400	0.00	N	. . .	. . .	1
HD 206893	F5V	6.69	38.3	−0.06	1, 18	4.25	6520	0.00	N	. . .	. . .	1
HD 207889	F5	7.20	49.6	−0.11	1	4.25	6520	0.00	N	. . .	. . .	1
HD 210210	F1IV	6.08	88.2	. . .	. . .	3.75	7100	0.00	N	. . .	. . .	1
HD 213429	F7V	6.15	25.4	−0.01	1, 19	4.25	6040	0.00	Y	0.072	6	1
HD 213617	F1V	6.43	50.3	−0.11	1	4.25	7020	0.00	N	. . .	. . .	1
HD 218980	F	8.58	(105.0)	. . .	. . .	4.25	7060	0.43	N	. . .	. . .	1
HD 221853	F0	7.35	68.4	−0.05	1, 18	4.25	6760	0.00	N	. . .	. . .	1

Notes. Column 1: identification. Column 2: spectral type. Column 3: V magnitude. Column 4: distance. Parentheses indicate photometric distances, otherwise *Hipparcos* distances from van Leeuwen (2007) are used. Column 5: metallicity. Literature data are used; if more than one observation is available the average of the [Fe/H] is quoted. Column 6: references for metallicity data. (1) Holmberg et al. (2007), (2) Gray et al. (2006), (3) Boesgaard et al. (1988b), (4) Takeda (2007), (5) Edvardsson et al. (1993), (6) Berthet (1990), (7) Cenarro et al. (2007), (8) Boesgaard (1987), (9) Friel & Boesgaard (1992), (10) Boesgaard & Tripicco (1986), (11) Balachandran (1990), (12) Boesgaard et al. (1988a), (13) Valenti & Fischer (2005), (14) Monier (2005), (15) Boesgaard & Friel (1990), (16) Reddy et al. (2003), (17) Metallicity was derived based on *uvby* (Hauck & Mermilliod 1997) photometric data, using the calibration described by Holmberg et al. (2007). (18) Saffe et al. (2008), (19) Boesgaard et al. (2004). Column 7: surface gravity values fixed in the course of fitting stellar atmospheric models. Column 8: derived effective temperature. Column 9: interstellar extinction. Column 10: multiplicity. Column 11: separation of the components if the object is in multiple system. Column 12: references for multiplicity data. (1) See Section 4.5. (2) Frankowski et al. (2007), (3) Dommanget & Nys (2002), (4) Balega et al. (2007), (5) Batten & Morbey (1980), (6) Pourbaix (2000). Column 13: selection criteria: (1) the star was suspected to display IR excess based on earlier IR observations; (2) the star was selected because of its kinematic group membership.

place the star at the center of the slit with a radial pointing uncertainty of $0''.4$ or $0''.14$, respectively. For most WDCs/ MGMs and for some CDCs the full wavelength coverage was requested (all four IRS modules were used), while in the remaining cases the shortest wavelength module (SL2, 5.2–7.4 μm) was dropped. In the case of HD 122106 and HD 125451, where no high accuracy peak-up observations were available, only the longest wavelength modules (LL2, LL1) were utilized (at long wavelengths the slit is larger and therefore the probability of loosing flux due to inaccurate position is expected to be lower). For the two brightest sources (HD 15745, HD 170773) low-resolution MIPS SED spectra (55–95 μm; $\lambda/\Delta\lambda \sim 15$–25) were also obtained. Six observing cycles were performed in both cases. Each cycle provided six pairs of 10 s long on- and off-source exposures. The on- and off-positions were separated by $2'$.

3.1. MIPS

3.1.1. Image Processing

The processing of MIPS data started from the Spitzer Science Center (SSC) basic calibrated data (BCD) produced by the pipeline version S16.1. Additional processing steps, including a flat-field correction and a background matching at 24 μm, were performed using MOsaicking and Point source Extraction (MOPEX, Makovoz & Marleau 2005). At 70 μm, column mean subtraction and time filtering were applied for the images following the steps recommended by Gordon et al. (2007). Finally, the improved BCD data were co-added and corrected for array distortions. Bad data flagged in the BCD mask files,

as well as permanently damaged pixels flagged in the static pixel mask file, were discarded during the data combination. Outlier pixels were rejected using a 5σ, 3σ, and 3σ clipping thresholds at 24 μm, 70 μm, and 160 μm, respectively. Output mosaics had pixels with sizes of $2''.5$, $4''$, and $8''$ at 24 μm, 70 μm, and 160 μm, respectively. The data reduction of the MIPS SED observations was also started with the BCD images (pipeline version S16.1), and the MOPEX was utilized to perform the necessary processing steps (combination of data, background removal, and application of dispersion solution) and to compile the final image with pixel size of $9''.8$.

3.1.2. Photometry

We used a modified version of the IDLPHOT routines to detect sources and to obtain photometry on the mosaic images.

MIPS 24. All of our sources were detected with good signal-to-noise ratio (S/N $\gtrsim$ 20) on the final 24 μm images. Figure 1 shows the positional offsets between the obtained centroids of the identified point sources and the Two Micron All Sky Survey (2MASS) position (corrected for the proper motion between the epochs of the two observations). None of the sources show more than 3σ deviations from the averaged position. Apart from HD 38905—offset of $1''.42$ from its 2MASS position—the angular offsets between the different positions are within the 1σ uncertainty ($\sim$$1''.4$) of the pointing reconstruction at 24 μm (see MIPS Instrument Handbook). Thus, we verify that the observed 24 μm emission is emerging from our targets.

Aperture photometry was performed to estimate the flux densities of the targets. The aperture was placed at the measured
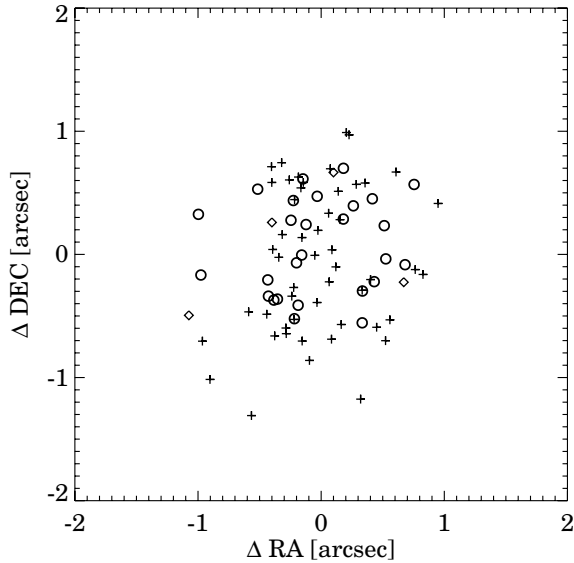
Figure 1. Offset between the source positions at $24\,\mu$m and the 2MASS position (after correcting for proper motion due to the time difference between the observations). Plus signs indicate stars with pure photospheric emission, circles show stars exhibiting excess at one or more MIPS wavelengths, while targets surrounded by bright extended nebulosity at $24\,\mu$m and/or $70\,\mu$m are represented by diamonds. The distributions of the offsets for stars with and without excess are in agreement within their formal uncertainties.
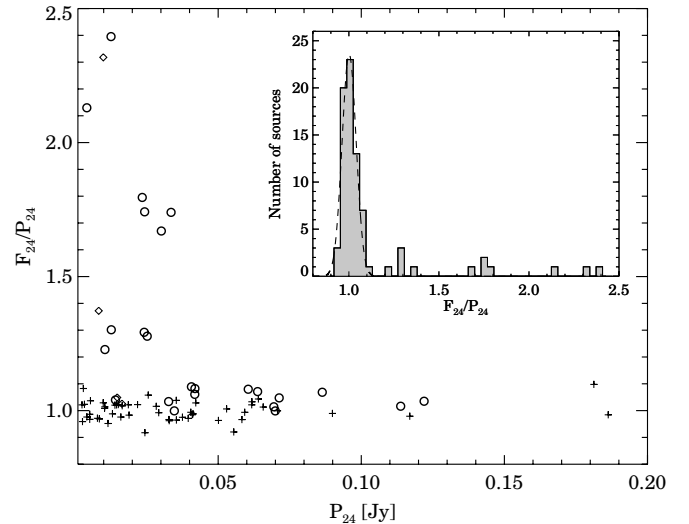

Figure 2. Flux ratio of the measured to the predicted flux densities as a function of the predicted photospheric fluxes for our sample stars measured at $24\,\mu$m with MIPS. For symbols see the caption of Figure 1. Small panel: the histogram of the flux ratio. The peak at around unity can be fitted by a Gaussian with a mean of 1.00 and dispersion of 0.038 (dashed line). We note that the disks around HD 15745, HD 35841, and HD 221853 with flux ratios of 9.79, 3.39, and 3.87, respectively, are out of the displayed range.

centroid of the source. The aperture radius was set to $13''$ and the background was computed in a sky annulus between $20''$ and $32''$. In the course of the sky estimates, we used an iterative sigma-clipping method, where the clipping threshold was set to 3σ. An aperture correction factor appropriate for a stellar photosphere was taken from Engelbracht et al. (2007). In some special cases we had to deviate from this standard method. For four sources (HD 36248, HD 143840, HD 185053, and HD 218980) that are surrounded by nebulosity at $24\,\mu$m or/and at $70\,\mu$m, a smaller aperture with radius of $3''.5$ was used. In cases where a bright nearby source contaminated the aperture photometry (HD 34739, HD 38905, HD 145371, and HD 184169), we performed point-spread function (PSF) photometry. The model PSF was constructed following Engelbracht et al. (2007). The uncertainties of the photometry were computed by adding quadratically the internal error and the absolute calibration uncertainty of 4% (MIPS Data Handbook). Due to the fact that our targets were measured with high S/N in this band, the uncertainty of the absolute calibration dominates the error budget. The resulting $24\,\mu$m photometry is presented in Table 2.

Figure 2 shows the distribution of flux ratios—measured flux densities (F_{24}) relative to the predicted fluxes (P_{24})—at $24\,\mu$m as the function of the predicted photospheric fluxes. The histogram of the F_{24}/P_{24} ratios shows a peak at around unity with a mean of 1.00 and dispersion of 0.038. The obtained dispersion is consistent with the quoted absolute calibration uncertainty. Stars with $F_{24}/P_{24} > 1.12$ have excess emission at this wavelength.

MIPS 70. At $70\,\mu$m 30 among our 82 targets were detected at $\geqslant 4\sigma$ level.

Aperture photometry with an aperture of $16''$ and sky annulus between $39''$ and $65''$ in radius was performed for all 82 targets. The sky level was estimated using the 3σ clipped mean. For the detected sources the aperture was placed around the derived centroid of the object, while in the remaining cases the $24\,\mu$m positions were used as the target coordinates. An aperture correction factor appropriate for a stellar photosphere

was taken from Gordon et al. (2007). After identifying stars with $70\,\mu$m excess, we recalculated their fluxes with an aperture correction appropriate for a 60 K blackbody (characteristic temperature of our disks). There are 11 images where bright nearby sources contaminated the photometry of our targets (see Notes in Table 2). In order to remove the contribution of these background objects, we fitted a PSF to them and then subtracted their emission (the PSF was constructed based on the method described by Gordon et al. 2007). For stars surrounded by bright extended nebulosity in the $70\,\mu$m images (HD 36248, HD 143840, HD 185053, and HD 218980), no photometry was derived. Due to the resampling of $70\,\mu$m mosaics, the noise between the adjacent pixels became correlated. In order to take into account this effect, in the course of internal photometric error estimation, we followed the method described by Carpenter et al. (2008). The resulting $70\,\mu$m photometry is presented in Table 2.

Positional offsets between the obtained centroids of the detected sources and their 2MASS positions as a function of S/N ($F_{70}/\sigma_{70}^{\mathrm{int}}$) measured at $70\,\mu$m are displayed in Figure 3. Most of our detected $70\,\mu$m sources are within $1''.7$ ($\sim1\sigma$ pointing reconstruction accuracy at $70\,\mu$m; MIPS Instrument Handbook) of the corresponding stellar positions. It is worth noting that even in the case of HD 14691—which shows the largest angular offset—the measured flux density is in good agreement with the predicted photospheric flux density at $70\,\mu$m, confirming the association between the $70\,\mu$m source and the star. It is thus probable that all of the detected sources are likely to be associated with our target stars.

Figure 4 shows the histogram of the significances of the differences between the measured and predicted photospheric flux densities, defined as $(F_{70} - P_{70})/\sigma_{70}^{\mathrm{int}}$, for all of our 78 targets (nebulous objects were excluded). The peak around zero significance level corresponds to either stars that have not been detected at this wavelength or objects that show pure photospheric emission. A Gaussian fit to this peak yields a mean of -0.09 and a dispersion of 0.87, and these parameters are

Table 2
MIPS Photometry

Source ID	AOR KEY	24 μm			70 μm			160 μm			Notes
		F_{24} (mJy)	P_{24} (mJy)	χ_{24}	F_{70} (mJy)	P_{70} (mJy)	χ_{70}	F_{160} (mJy)	P_{160} (mJy)	χ_{160}	
HD 3670	15010816	12.8 ± 0.5	10.4	3.9	134.9 ± 10.4	1.1	12.8	77.2 ± 13.4	0.2	5.7	
HD 14691	14996736	114.4 ± 4.5	116.9	−0.4	17.7 ± 5.0	12.7	0.9	. . .	. . .	. . .	
HD 15060	23050496	34.6 ± 1.3	34.6	−0.0	14.8 ± 3.5	3.7	3.1	. . .	. . .	. . .	
HD 15115	10885888	58.3 ± 2.3	33.5	9.7	451.9 ± 32.6	3.6	13.7	217.3 ± 27.8	0.7	7.7	
HD 15745	10886400	169.4 ± 6.7	17.3	22.3	741.0 ± 52.6	1.8	14.0	230.8 ± 29.9	0.3	7.6	
HD 16743	15002624	50.3 ± 2.0	30.1	9.1	368.8 ± 26.5	3.2	13.7	174.7 ± 24.5	0.6	7.0	5
HD 17390	10887168	45.3 ± 1.8	41.8	1.5	255.2 ± 18.9	4.5	13.2	210.0 ± 28.3	0.9	7.3	
BD+49° 896	15008000	2.4 ± 0.1	2.6	−0.5	0.5 ± 4.9	0.2	0.0	. . .	. . .	. . .	
HD 20759	23051008	19.0 ± 0.7	18.6	0.4	9.6 ± 4.0	2.0	1.8	. . .	. . .	. . .	
HD 24636	23051520	42.3 ± 1.6	24.3	9.7	35.1 ± 4.7	2.6	6.8	. . .	. . .	. . .	
HD 25570	15002880	115.6 ± 4.6	113.7	0.3	170.5 ± 13.3	12.4	11.8	115.0 ± 28.4	2.5	3.9	6
HD 25953	15009792	16.7 ± 0.6	16.4	0.3	−5.0 ± 4.4	1.8	−1.5	−6.3 ± 41.3	0.3	−0.1	
HD 27429	14996992	63.8 ± 2.5	61.7	0.6	6.8 ± 6.9	6.7	0.0	. . .	. . .	. . .	
HD 30447	10887680	30.1 ± 1.2	12.5	13.8	289.8 ± 21.1	1.3	13.6	120.3 ± 17.6	0.2	6.8	
HD 32195	15009536	16.4 ± 0.6	12.6	4.9	17.0 ± 3.9	1.3	3.9	−21.3 ± 20.3	0.2	−1.0	
HD 30743	15003136	66.6 ± 2.6	65.7	0.2	13.9 ± 7.5	7.2	0.8	5.4 ± 17.2	1.4	0.2	5, 6
HD 33081	14997248	33.8 ± 1.3	32.6	0.6	35.8 ± 5.1	3.5	6.2	. . .	. . .	. . .	
HD 33276	15003392	198.9 ± 7.9	181.2	1.8	26.8 ± 9.2	19.6	0.7	50.9 ± 42.5	4.0	1.1	6
HD 34739	10888192	4.0 ± 0.1	4.1	−0.4	−1.7 ± 4.9	0.4	−0.4	. . .	. . .	. . .	2, 3, 4
HD 35114	11260160	32.2 ± 1.2	25.2	4.6	20.2 ± 4.2	2.7	4.0	. . .	. . .	. . .	
HD 35841	15011840	18.4 ± 0.7	5.4	17.0	172.1 ± 13.6	0.5	12.5	37.5 ± 14.2	0.1	2.6	
HD 36248	14997504	16.8 ± 0.6	16.3	0.4	. . .	. . .	. . .	. . .	. . .	. . .	1
HD 36968	15012096	8.7 ± 0.3	4.1	12.1	148.1 ± 12.5	0.4	11.7	105.0 ± 16.6	0.09	6.3	5
HD 37402	15011072	10.4 ± 0.4	10.3	0.1	−1.6 ± 4.2	1.1	−0.6	−19.5 ± 12.0	0.2	−1.6	5
HD 38905	15012352	3.1 ± 0.1	2.9	1.3	−0.2 ± 7.4	0.3	−0.0	. . .	. . .	. . .	2, 3, 4
HD 47412	14997760	38.3 ± 1.5	39.5	−0.5	5.8 ± 5.4	4.3	0.2	. . .	. . .	. . .	
HD 48391	15010048	15.6 ± 0.6	16.0	−0.4	17.1 ± 5.6	1.7	2.7	−26.9 ± 20.5	0.3	−1.3	
HD 50571	15003904	70.4 ± 2.8	69.4	0.2	248.8 ± 18.7	7.5	12.8	214.6 ± 36.0	1.5	5.9	6, 7
HD 55003	23054848	31.6 ± 1.2	32.9	−0.7	2.5 ± 3.6	3.5	−0.2	. . .	. . .	. . .	
HD 56099	15004160	22.3 ± 0.8	21.8	0.4	10.6 ± 7.6	2.3	1.0	. . .	. . .	. . .	3, 4
HD 58853	15004416	5.0 ± 0.2	5.1	−0.2	6.6 ± 6.5	0.5	0.9	. . .	. . .	. . .	3, 4
HD 61518	15010304	15.4 ± 0.6	15.1	0.4	−9.0 ± 5.4	1.6	−1.9	3.9 ± 17.2	0.3	0.2	
HD 67587	14998016	56.3 ± 2.2	58.3	−0.6	12.9 ± 9.6	6.3	0.6	. . .	. . .	. . .	
HD 69351	14998272	31.7 ± 1.2	32.8	−0.6	−1.6 ± 5.9	3.5	−0.8	. . .	. . .	. . .	
HD 79873	14998528	40.7 ± 1.6	41.2	−0.2	−2.1 ± 4.8	4.4	−1.3	. . .	. . .	. . .	
HD 82821	15004672	7.5 ± 0.3	7.8	−0.5	4.0 ± 8.0	0.8	0.3	−4.5 ± 13.3	0.1	−0.3	5
HD 86146	14998784	183.3 ± 7.3	186.2	−0.3	21.4 ± 4.6	20.2	0.2	. . .	. . .	. . .	
PPM 7774	15011584	4.9 ± 0.2	5.1	−0.6	−0.3 ± 7.3	0.5	−0.1	−90.6 ± 43.5	0.1	−2.0	5
HD 103257	14999040	36.7 ± 1.4	35.3	0.7	12.7 ± 7.3	3.8	1.2	. . .	. . .	. . .	
HD 107067	15008768	8.2 ± 0.3	8.4	−0.6	−5.4 ± 10.6	0.9	−0.6	−21.5 ± 10.4	0.1	−2.0	
HD 108102	15009024	14.2 ± 0.5	13.9	0.3	−0.0 ± 7.0	1.5	−0.2	21.9 ± 11.6	0.3	1.8	
HD 113337	14999296	74.7 ± 2.9	71.3	0.9	178.2 ± 13.3	7.7	12.7	. . .	. . .	. . .	
HD 114905	14999552	40.3 ± 1.6	40.9	−0.3	3.1 ± 4.1	4.4	−0.3	. . .	. . .	. . .	
HD 117360	19890432	51.0 ± 2.0	55.4	−1.6	6.6 ± 6.0	6.0	0.0	. . .	. . .	. . .	
HD 120160	15004928	14.6 ± 0.6	14.1	0.7	30.7 ± 7.3	1.5	3.9	1.2 ± 22.7	0.3	0.0	
HD 122106	15005184	58.8 ± 2.3	59.2	−0.1	1.8 ± 7.7	6.4	−0.5	. . .	. . .	. . .	4
HD 122510	15000064	70.6 ± 2.8	70.7	−0.0	8.8 ± 5.3	7.7	0.2	. . .	. . .	. . .	
HD 124988	23062016	28.8 ± 1.1	28.3	0.3	9.7 ± 4.1	3.0	1.5	. . .	. . .	. . .	
HD 125451	15008256	126.2 ± 5.0	121.9	0.6	64.6 ± 8.1	13.2	6.3	−2.0 ± 11.2	2.7	−0.4	6
HD 127821	15005440	69.8 ± 2.7	69.9	−0.0	360.3 ± 25.9	7.6	13.5	295.5 ± 37.2	1.5	7.8	6
HD 131495	15000320	34.1 ± 1.3	35.4	−0.7	−4.8 ± 4.8	3.8	−1.8	. . .	. . .	. . .	
HD 134150	10888960	2.4 ± 0.1	2.4	0.3	−6.5 ± 7.4	0.2	−0.9	3.5 ± 15.7	0.05	0.2	5
HD 136580	15000576	40.1 ± 1.6	40.4	−0.1	−0.9 ± 4.2	4.4	−1.2	. . .	. . .	. . .	
HD 136407	15005696	66.8 ± 2.6	64.0	0.8	10.3 ± 7.9	6.9	0.4	−6.0 ± 22.8	1.4	−0.3	6
HD 138100	15000832	36.5 ± 1.4	37.5	−0.5	0.8 ± 4.2	4.0	−0.7	. . .	. . .	. . .	
HD 139798	15008512	88.9 ± 3.5	89.9	−0.2	10.7 ± 5.9	9.8	0.1	−20.7 ± 10.6	2.0	−2.1	6
HD 143840	10889472	15.4 ± 0.6	14.7	0.9	. . .	. . .	. . .	. . .	. . .	. . .	1
HD 145371	15007744	3.3 ± 0.1	3.2	0.4	0.1 ± 7.4	0.3	−0.0	. . .	. . .	. . .	2, 3, 4
HD 151044	10890240	68.3 ± 2.7	63.7	1.3	95.6 ± 7.9	6.9	11.2	47.4 ± 11.7	1.4	3.9	6
HD 153377	15005952	18.5 ± 0.7	18.8	−0.3	−2.0 ± 5.6	2.0	−0.7	26.9 ± 24.0	0.4	1.1	
HD 155990	15010560	14.8 ± 0.6	14.5	0.4	5.7 ± 5.1	1.5	0.8	. . .	0.3	2.3	4
HD 156635	15006208	48.2 ± 1.9	50.1	−0.7	6.9 ± 6.1	5.4	0.2	56.7 ± 75.4	1.1	0.7	
HD 170773	10890752	65.3 ± 2.6	60.5	1.5	787.9 ± 56.0	6.6	13.9	692.3 ± 83.8	1.3	8.2	6, 7
HD 184169	10891264	10.5 ± 0.4	10.3	0.2	−12.1 ± 12.4	1.1	−1.0	. . .	. . .	. . .	2, 3, 4
HD 183577	15001600	63.0 ± 2.5	61.7	0.4	4.8 ± 4.6	6.7	−0.4	. . .	. . .	. . .	

Source ID	AOR KEY	24 μm			70 μm			160 μm			Notes
		F_{24} (mJy)	P_{24} (mJy)	χ_{24}	F_{70} (mJy)	P_{70} (mJy)	χ_{70}	F_{160} (mJy)	P_{160} (mJy)	χ_{160}	
HD 185053	10892032	22.8 ± 0.9	9.8	13.4	. . .	. . .	. . .	. . .	. . .	. . .	1
HD 189207	15006464	10.1 ± 0.4	9.8	0.5	5.9 ± 5.4	1.0	0.8	−46.4 ± 30.6	0.2	−1.5	
HD 192486	15001856	43.3 ± 1.7	42.1	0.5	−5.2 ± 4.6	4.6	−2.1	. . .	. . .	. . .	
HD 192758	10892800	42.1 ± 1.6	23.4	10.1	452.4 ± 32.5	2.5	13.8	200.7 ± 26.3	0.5	7.5	
HD 195952	15006720	12.9 ± 0.5	13.0	−0.2	1.4 ± 8.1	1.4	0.0	. . .	. . .	. . .	3, 4
HD 199391	15006976	22.3 ± 0.9	24.4	−1.7	−7.5 ± 10.2	2.6	−0.9	130.7 ± 27.8	0.5	4.6	5
PPM 171537	15011328	5.5 ± 0.2	5.3	0.6	−2.4 ± 7.7	0.5	−0.3	. . .	. . .	. . .	3, 4
HD 204942	15007232	10.9 ± 0.7	11.5	−0.6	−13.8 ± 11.0	1.2	−1.3	. . .	. . .	. . .	3, 4
HD 205674	15007488	31.2 ± 1.2	24.1	4.8	232.5 ± 17.9	2.6	12.8	185.6 ± 26.4	0.5	6.9	
HD 206554	23067648	29.0 ± 1.1	29.2	−0.1	1.4 ± 6.3	3.1	−0.2	. . .	. . .	. . .	3
HD 206893	10893312	44.2 ± 1.7	40.6	1.6	265.7 ± 20.0	4.4	13.0	193.1 ± 26.2	0.9	7.3	
HD 207889	23068160	27.0 ± 1.0	25.5	1.1	4.7 ± 3.8	2.7	0.4	. . .	. . .	. . .	3
HD 210210	15002112	53.2 ± 2.1	52.9	0.1	5.0 ± 4.0	5.7	−0.1	. . .	. . .	. . .	
HD 213429	21840896	92.2 ± 3.6	86.3	1.3	22.2 ± 4.1	9.4	3.0	. . .	. . .	. . .	
HD 213617	10893824	44.3 ± 1.7	41.8	1.1	119.2 ± 10.0	4.5	11.3	96.4 ± 22.9	0.9	4.1	5
HD 218980	13238784	11.3 ± 0.4	8.2	5.9	. . .	. . .	. . .	. . .	. . .	. . .	1
HD 221853	10894848	78.5 ± 3.2	20.3	17.7	336.5 ± 24.7	2.2	13.5	105.3 ± 20.4	0.4	5.1	

Notes. Column 1: identification. Column 2: AOR Key for MIPS measurement. Using the AOR key one can query additional details for each observation (e.g., measurement setups) from the *Spitzer* Data Archive at the Spitzer Science Center. Columns 3–11: measured and predicted flux densities with their uncertainties and the significance of the excesses at 24/70/160 μm. The quoted uncertainties include the calibration uncertainties as well. Column 12: Notes. 1: nebulosity. At 24 μm a small aperture with 3″5 radius was used. At 70 μm and 160 μm no photometric values were quoted; 2: A bright nearby source contaminated the aperture photometry at 24 μm—PSF photometry was used; 3: Bright nearby sources contaminated the photometry of our target at 70 μm. In order to remove the contribution of these background objects, we fitted PSF to these sources and subtracted their emission before the photometry for our target was performed. 4: Nearby bright object at 160 μm in the aperture—no photometry is given; 5: A bright nearby source contaminated the annulus at 160 μm. The background source was masked out in the course of photometry; 6: The ghost image was subtracted at 160 μm before the photometry was performed. 7: The source is marginally extended at 70 μm and the photometry was derived using the fitted profile (see Section 4.3).
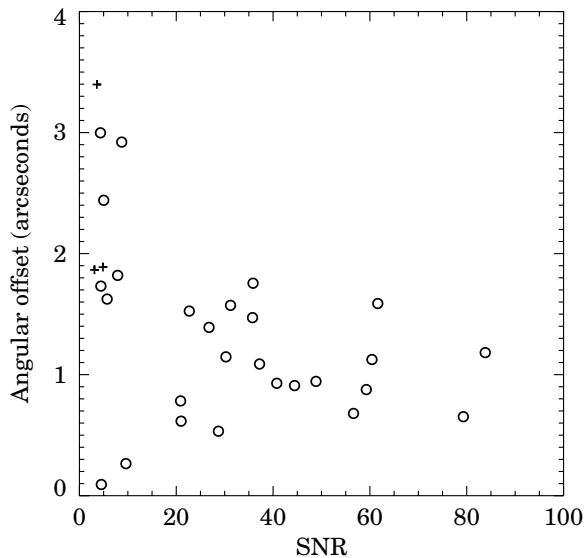
Figure 3. Positional offsets between the centroids of point sources detected at 70 μm and the 2MASS position (after correcting for proper motion due to the time difference between the observations) as a function of the signal-to-noise ratio measured at 70 μm. For symbols see the caption of Figure 1. Apart from HD 14691, HD 48391, and HD 86146 all of the detected sources exhibit excess emission at 70 μm.

Figure 4. Histogram of the significances of the differences between the measured and predicted photospheric flux densities, defined as $(F_{70} - P_{70})/\sigma_{70}^{int}$, for targets measured at 70 μm. Small panel: a zoom for the peak at zero. A Gaussian fit to the peak provides a mean of −0.09 and a dispersion of 0.87, in good agreement with the expectations.

in good agreement with the expectations (mean of 0.0 with dispersion of 1.0).

The total noise in the photometry was derived as the quadratic sum of the internal and the absolute calibration uncertainties (7%; see MIPS Data Handbook).

MIPS 160. MIPS 160 μm observations suffer from a spectral leak resulting in a ghost image at a certain offset from the nominal position of the original target (e.g., Stansberry et al. 2007). According to the MIPS Data Handbook (ver. 3.2) the ghost is bright enough to appear above the confusion noise only for sources brighter than 5.5 mag in *J* band. For those of our targets (10 objects, see Table 2 for details) that are brighter than this limit, we applied the procedure proposed by Tanner et al. (2009) to minimize the contamination of the leak image. We downloaded from the *Spitzer* Archive 24 μm and 160 μm BCD level data for 13 bright stars listed in Table 2 of

Tanner et al. (2009) that have no excess in MIPS bands. These data were processed identically to our F-stars observations (see Section 3.1.1). On the final images we determined the average offset of the ghost images from the position of the stars (obtained at 24 μm images), yielding 5 and 0.2 pixels in the *X*- and *Y*-directions, respectively, in good agreement with Tanner et al. (2009). Then we compiled the typical PSF of the leak image using the ghost images of the brightest four stars. As a final step, utilizing the leak PSF and the estimated offset position of the ghost image, we applied an iterative cleaning method to remove the leak from the 160 μm images of our brightest F stars. We performed aperture photometry to obtain flux measurements on MIPS 160 μm images. The aperture was centered on the source positions obtained on the 24 μm images. The aperture radius was set to 32″, the background level was estimated using an iterative clipping procedure in an annulus extending from 64″ to 128″. We used an aperture correction factor corresponding to a 50 K temperature blackbody (Stansberry et al. 2007). For those stars where extended nebulosity or a nearby bright source contaminated the area of the aperture, we give no photometry at 160 μm in Table 2. In some cases, nearby bright sources appear in the background annulus. To minimize their influence, we placed a 4 pixel radius mask on these sources before we estimated the sky level (see Table 2 for the affected sources).

MIPS SED. Two of our targets, HD 50571 and HD 170773 were observed in MIPS SED mode as well. The spectra were extracted from the sky-subtracted mosaic images using a 5 pixel wide aperture. Aperture correction was needed to correct for flux losses. Although HD 170773 is slightly extended at 70 μm (see Section 4.3), our studies based on smoothed *Spitzer* TinyTim models of the MIPS SED PSF (Krist 2002; Lu et al. 2008) showed that the difference in aperture corrections between a point source and a point source convolved by a Gaussian with FWHM of 10″ is insignificant. Thus, we applied aperture correction factors valid for point sources (Lu et al. 2008) for both stars. We discarded the longest wavelength part of both spectra (λ > 90 μm) because of their very low S/N. As a final step of the data processing, we scaled our spectra to the photometry obtained in the 70 μm band as follows (the MIPS SED and MIPS photometric observations were performed on the same day). We extrapolated the spectra toward both shorter and longer wavelengths based on IRS and 160 μm photometry, in order to completely cover the transmission curve of the MIPS 70 μm filter. We computed synthetic 70 μm photometry and derived the ratio of the synthetic to the measured flux density. According to the resulting ratios, the MIPS SED of HD 15745 and HD 170773 were scaled down by 1.11 and 1.16, respectively.

3.2. IRS

The reduction of the IRS observations started from the so-called *droopres* products (see the IRS Instrument Handbook) of the SSC pipeline (version S15.3). We used the SMART reduction package (Higdon et al. 2004), in combination with IDL routines developed for the FEPS Spitzer Science Legacy program (Meyer et al. 2006). We first subtracted the pairs of imaged spectra acquired along the spatial direction of the slit to correct for background emission, stray light, and pixels with anomalous dark current. We replaced bad pixels by interpolating over neighboring good pixels. Spectra were extracted from the background-subtracted pixel-corrected images using a 6 pixel fixed-width aperture in the spatial direction centered at the position derived by the FEPS Legacy program. After extracting the spectra for each order, nod, and cycle, we computed a mean
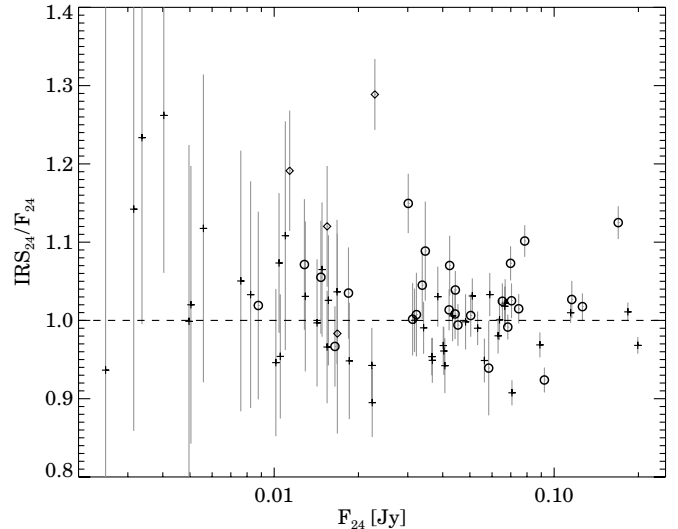
Figure 5. Ratio of the synthetic IRS 24 μm photometry to the MIPS photometry at 24 μm as a function of the MIPS flux densities. For symbols see the caption of Figure 1. The mean of the IRS_{24}/F_{24} ratios is 1.02 with a dispersion of 0.06. The dashed line corresponds to the IRS_{24}/F_{24} ratio of 1.

spectrum for each order, and as uncertainty we quoted the 1σ standard deviation of the distribution of the flux densities measured at the given wavelength. We converted our output spectra to flux units by applying the spectral response function derived by the FEPS Legacy team (Bouwman et al. 2008) and propagate the calibration error into the quoted uncertainties.

Using the filter transmission curve of the MIPS 24 μm band we computed synthetic photometry from the IRS spectra (IRS_{24}) for all of the targets. Figure 5 shows a comparison between the synthetic IRS 24 μm and the measured MIPS 24 μm flux densities (F_{24}). The calibration of the two instruments shows good agreement in general, the mean of the IRS_{24}/F_{24} ratios is 1.02 with a dispersion of 0.06. The largest discrepancy between the two instruments (∼30%) was found at HD 185053, a source surrounded with extended nebulosity.

3.3. Additional Data

For the targets where the *Spitzer* observations pointed to the existence of excess emission (Section 4.1), we collected additional infrared and submillimeter data from the literature. *IRAS* 60 μm and 100 μm flux densities and their uncertainties were taken from the *IRAS* FSC (Moshir et al. 1989). Williams & Andrews (2006) detected three of our targets (HD 15115, HD 127821, and HD 206893) at 850 μm using the JCMT/ SCUBA instrument, while Nilsson et al. (2010) observed three sample stars (HD 17390, HD 30447, and HD 170773) at 870 μm with the LABOCA/APEX instrument.

Observations obtained with ISOPHOT, the photometer on board the *ISO* were available for 10 sources. We observed three northern stars with the IRAM 30 m telescope at millimeter wavelengths. Moreover, for some targets we performed optical spectroscopy. In the following we describe the details of the data processing.

3.3.1. ISO/ISOPHOT

Ten out of the 27 objects with confirmed infrared excess were observed with ISOPHOT as well. For eight of these ten stars, there are published ISOPHOT fluxes in Moór et al. (2006). For the remaining two objects, HD 151044, HD 213617, we

Table 3
Additional Photometric Data

Source ID	Instrument	Wavelength (μm)	F_ν (mJy)
HD 151044	*ISO*/ISOPHOT	60	111.0 $\pm$ 13.0
HD 151044	*ISO*/ISOPHOT	90	101.0 $\pm$ 10.0
HD 170773	*ISO*/ISOPHOT	60	570.0 $\pm$ 35.0
HD 170773	*ISO*/ISOPHOT	90	771.0 $\pm$ 54.0
HD 213617	*ISO*/ISOPHOT	60	110.0 $\pm$ 13.0
HD 213617	*ISO*/ISOPHOT	90	121.0 $\pm$ 14.0
HD 15745	IRAM/MAMBO2	1200	1.3 $\pm$ 0.6
HD 25570	IRAM/MAMBO2	1200	0.6 $\pm$ 0.6
HD 113337	IRAM/MAMBO2	1200	0.4 $\pm$ 0.3

processed the ISOPHOT data in the same way as described in that paper and the results are given in Table 3. HD 170773 was included in Moór et al. (2006), however, the photometric results were extracted assuming a point-like source. The analysis of our MIPS data showed that the disk around HD 170773 is spatially extended with an extent of $\sim$10$''$ (Section 4.3). Assuming that the spatial extent of the disk is similar at 60 μm and 90 μm, we re-analyzed the ISOPHOT data by convolving the appropriate ISOPHOT beam profiles by a Gaussian with FWHM of $\sim$10$''$ and then using this new profile in the course of the flux extraction. The new photometry is given in Table 3.

3.3.2. IRAM/MAMBO2

We observed three stars (HD 15745, HD 25570, and HD 113337) at 1.2 mm using the IRAM 30 m telescope at Pico Veleta with the 117 element MAMBO2 bolometer (proposal ID: 195/07, PI: A. Moór). None of them have been observed at millimeter wavelengths before. The observations were carried out between 2007 December and 2008 April, using the standard on–off observing mode. The targets were always positioned on pixel 20 (the most sensitive bolometer pixel). Observations of Mars were used to establish the absolute flux calibration. The value of the zenith opacity at 1.2 mm ranged between 0.17 and 0.48 during our observations. We performed 3, 3, and 11 of 20 minutes long ON–OFF scan blocks for HD 15745, HD 25570, and HD 113337, respectively. We utilized the

MOPSIC software package (R. Zylka) to perform the data processing using the standard scripts developed for the reduction of on–off observation data with sky noise subtraction. None of our targets were detected at 3σ level. The obtained flux densities and their uncertainties are quoted in Table 3.

3.3.3. Ground Based Spectroscopy

In 2009 July and August, we obtained new high-resolution optical spectroscopy for stars in Table 4, using the 2.3 m telescope and the Echelle spectrograph of the Australian National University. The total integration time per object ranged from 30 s to 1800 s, depending on the target brightness. The spectra covered the whole visual range in 27 echelle orders between 3900 Å and 6720 Å , with only small gaps between the three reddest orders. The nominal spectral resolution is $\lambda/\Delta\lambda \approx 23$ 000 at the Hα line, with typical S/N of about 100.

All data were reduced with standard IRAF[12] tasks, including bias and flat-field corrections, cosmic-ray removal, extraction of the 27 individual orders of the echelle spectra, wavelength calibration, and continuum normalization. ThAr spectral lamp exposures were regularly taken before and after every object spectrum to monitor the wavelength shifts of the spectra on the CCD. We also obtained spectra for the telluric standard HD 177724 and IAU radial velocity (RV) standards β Vir (sp. type F9V) and HD 223311 (K4III).

The spectroscopic data analysis consisted of two main steps. First, we measured radial velocities by cross-correlating the target spectra (using the IRAF task *fxcor*) with that of the RV standard that matched the spectral type of the target— β Vir was used for the F-type targets and HD 223311 for the lone late G-type target (SAO 232842). Each spectral order was treated separately and the resulting velocities and the estimated uncertainties were calculated as the means and the standard deviations of the velocities from the individual orders. For most of the targets, the two IAU standards gave velocities within 0.1–0.5 km s^{-1}, which is an independent measure of the absolute uncertainties. The equivalent width of the 6708 Å Li were

---

[12] IRAF is distributed by the National Optical Astronomy Observatory, which is operated by the Association of Universities for Research in Astronomy, Inc., under cooperative agreement with the National Science Foundation.

Table 4
Additional Spectroscopic Information and Derived Kinematic Properties

Source ID	v_r (km s^{-1})	U (km s^{-1})	V (km s^{-1})	W (km s^{-1})	$v \sin i$ (km s^{-1})	EW$_{Li}$ (mÅ)
HD 15745	2.5 $\pm$ 3.3	$-$10.4 $\pm$ 2.5	$-$15.3 $\pm$ 1.9	$-$7.9 $\pm$ 1.2	50	...
HD 16699	16.2 $\pm$ 0.2	$-$23.5 $\pm$ 1.5	$-$15.0 $\pm$ 0.4	$-$10.3 $\pm$ 0.3	20	40 $\pm$ 10
SAO 232842	15.8 $\pm$ 0.3	...	...	...	...	220 $\pm$ 10
HD 16743	17.3 $\pm$ 8.5	$-$23.3 $\pm$ 0.5	$-$15.4 $\pm$ 4.6	$-$11.3 $\pm$ 7.2	100	...
HD 24636	14.0 $\pm$ 0.7	$-$8.8 $\pm$ 0.3	$-$20.5 $\pm$ 0.6	$-$1.6 $\pm$ 0.5	30	50 $\pm$ 10
HD 36968[a]	15.0 $\pm$ 2.0	$-$14.8 $\pm$ 2.1	$-$6.6 $\pm$ 2.0	$-$8.5 $\pm$ 1.3	...	...
HD 170773	$-$17.5 $\pm$ 1.5	$-$22.2 $\pm$ 1.5	$-$4.6 $\pm$ 0.2	$-$15.0 $\pm$ 0.5	50	...
HD 205674	$-$1.4 $\pm$ 1.3	$-$3.0 $\pm$ 0.8	$-$25.2 $\pm$ 1.1	$-$14.6 $\pm$ 1.1	30	20 $\pm$ 10
HD 206893	$-$11.8 $\pm$ 1.6	$-$19.2 $\pm$ 0.9	$-$7.2 $\pm$ 0.8	$-$2.7 $\pm$ 1.1	33	...
HD 221853	$-$8.4 $\pm$ 1.8	$-$11.9 $\pm$ 0.6	$-$22.4 $\pm$ 1.4	$-$7.3 $\pm$ 1.5	40	...

Notes. Column 1: identification. Column 2: heliocentric radial velocity. Columns 3–5: Galactic space velocity components of the star. In the calculation of the Galactic space velocity we used a right-handed coordinate system (U is positive toward the Galactic center, V is positive in the direction of galactic rotation, and W is positive toward the galactic North pole) and followed the general recipe described in "The *Hipparcos* and *Tycho* Catalogues" (ESA 1997). Column 6: projected rotational velocity. Column 7: measured lithium equivalent width.
[a] HD 36968 was measured in the framework of a previous program that carried out with the 2.3 m ANU telescope at the Siding Spring Observatory (Australia), using the Double Beam Spectrograph (for details see Moór et al. 2006).

Table 5
Synthetic IRS Photometry for Stars with Infrared Excess

Source ID	AOR KEY	Synthetic Photometry [mJy]										
		(8–10 μm)	(10–12 μm)	(12–14 μm)	(14–16 μm)	(16–18 μm)	(18–20 μm)	(20–23 μm)	(23–26 μm)	(26–29 μm)	(29–32 μm)	(32–35 μm)
HD 3670	15025664	71.8 ± 9.0	48.9 ± 5.0	35.8 ± 4.4	26.7 ± 2.6	20.1 ± 2.0	16.6 ± 2.5	14.7 ± 2.0	13.2 ± 1.0	14.1 ± 1.3	15.9 ± 1.4	20.9 ± 2.6
HD 15060	23050752	227.6 ± 30.4	149.9 ± 15.9	109.9 ± 10.0	89.4 ± 7.5	69.5 ± 6.1	53.2 ± 6.6	43.9 ± 5.8	33.3 ± 2.4	26.5 ± 2.1	21.3 ± 2.5	17.5 ± 3.7
HD 15115	10885632	218.0 ± 36.8	148.7 ± 15.6	111.2 ± 10.0	87.0 ± 7.7	70.8 ± 4.6	61.0 ± 2.3	53.7 ± 2.7	54.9 ± 2.5	60.3 ± 2.8	71.8 ± 5.1	93.5 ± 9.8
HD 15745	10886144	123.5 ± 15.8	83.9 ± 8.3	65.2 ± 4.1	67.7 ± 3.9	81.2 ± 7.5	110.2 ± 9.7	143.2 ± 19.2	218.9 ± 16.7	276.8 ± 19.4	335.2 ± 22.7	431.0 ± 30.5
HD 16743	15018240	208.5 ± 29.0	142.5 ± 15.0	105.9 ± 7.3	79.1 ± 6.0	62.9 ± 3.8	54.5 ± 2.9	50.7 ± 2.0	50.4 ± 1.8	52.3 ± 2.1	57.9 ± 3.0	70.4 ± 5.5
HD 17390	10886912	278.2 ± 30.6	196.6 ± 21.9	141.6 ± 12.9	103.7 ± 8.2	80.5 ± 5.3	63.3 ± 4.5	52.2 ± 4.2	42.8 ± 2.6	37.5 ± 1.7	36.2 ± 1.9	38.7 ± 3.0
HD 24636	23051776	163.1 ± 19.9	111.5 ± 11.1	84.2 ± 7.8	68.7 ± 4.3	57.4 ± 3.0	50.2 ± 3.3	46.6 ± 3.1	44.2 ± 1.4	43.6 ± 1.2	44.2 ± 1.9	44.0 ± 4.3
HD 25570	15018496	755.7 ± 143.7	530.2 ± 56.6	383.5 ± 36.7	285.3 ± 21.6	222.8 ± 16.0	178.1 ± 12.9	142.9 ± 13.5	111.2 ± 7.8	92.1 ± 4.6	79.0 ± 6.3	72.2 ± 6.6
HD 30447	10887424	83.0 ± 11.1	55.9 ± 5.8	41.7 ± 4.3	34.0 ± 2.5	29.1 ± 2.0	26.4 ± 2.5	28.5 ± 3.0	35.7 ± 1.9	45.2 ± 3.9	58.5 ± 5.4	80.4 ± 7.2
HD 32195	15024384	86.6 ± 10.7	58.8 ± 6.7	43.4 ± 4.2	31.5 ± 2.3	25.3 ± 2.3	20.6 ± 2.3	17.4 ± 2.1	15.5 ± 1.1	13.5 ± 1.1	11.9 ± 1.1	12.0 ± 2.0
HD 33081	15013120	219.5 ± 28.6	151.5 ± 16.1	109.3 ± 9.8	82.0 ± 5.9	64.3 ± 4.3	51.6 ± 5.4	41.7 ± 3.8	33.5 ± 2.1	27.6 ± 1.8	23.5 ± 1.8	20.2 ± 1.8
HD 35114	26362112	171.5 ± 25.5	110.1 ± 13.8	81.5 ± 8.4	62.3 ± 5.9	50.7 ± 3.3	40.8 ± 4.1	35.9 ± 3.5	29.9 ± 1.7	26.5 ± 1.9	24.1 ± 2.1	22.5 ± 4.7
HD 35841	15026688	36.8 ± 5.0	24.7 ± 3.0	17.7 ± 1.8	13.7 ± 1.3	11.6 ± 1.3	10.7 ± 1.7	13.4 ± 2.3	20.7 ± 3.0	28.4 ± 3.1	37.1 ± 3.3	50.7 ± 5.4
HD 36968	15026944	28.2 ± 3.4	19.4 ± 2.2	14.5 ± 1.7	9.9 ± 1.4	9.4 ± 1.3	7.3 ± 1.4	7.0 ± 1.7	9.3 ± 1.0	12.3 ± 1.6	17.2 ± 2.4	24.9 ± 3.9
HD 50571	15019520	422.2 ± 28.8	311.6 ± 34.2	225.3 ± 21.0	172.7 ± 12.3	134.0 ± 10.0	104.5 ± 7.0	84.5 ± 6.0	68.5 ± 5.0	56.6 ± 2.5	49.1 ± 3.3	50.7 ± 4.9
HD 113337	15015168	475.6 ± 64.0	321.6 ± 35.7	232.5 ± 21.1	176.5 ± 12.8	136.9 ± 9.6	108.5 ± 6.6	87.5 ± 7.7	72.8 ± 4.5	62.4 ± 1.9	57.4 ± 1.6	58.3 ± 3.8
HD 120160	15020544	94.9 ± 13.4	64.1 ± 6.8	46.0 ± 5.2	34.8 ± 3.0	27.4 ± 2.1	22.6 ± 2.1	17.9 ± 2.2	14.9 ± 1.3	12.7 ± 0.9	11.5 ± 0.9	12.1 ± 1.4
HD 125451	15027968	...	...	...	297.1 ± 18.8	235.7 ± 15.8	187.1 ± 12.5	152.4 ± 12.0	121.0 ± 6.3	98.9 ± 5.8	82.0 ± 5.4	73.2 ± 4.0
HD 127821	15020800	475.5 ± 63.2	319.8 ± 34.7	230.8 ± 21.9	176.1 ± 13.0	136.6 ± 9.7	108.9 ± 7.6	88.6 ± 7.5	71.3 ± 3.5	59.3 ± 2.5	53.9 ± 2.6	52.6 ± 4.3
HD 151044	10889984	411.6 ± 58.7	277.6 ± 26.0	209.1 ± 15.4	156.4 ± 15.3	120.2 ± 9.3	95.5 ± 4.5	77.5 ± 4.7	64.7 ± 4.1	54.6 ± 2.5	47.8 ± 2.4	47.0 ± 2.7
HD 170773	10890496	406.5 ± 53.6	276.6 ± 30.0	200.1 ± 19.1	149.5 ± 12.4	117.4 ± 9.4	94.5 ± 6.3	77.5 ± 6.4	63.6 ± 3.2	55.9 ± 1.8	54.6 ± 1.8	62.1 ± 3.4
HD 192758	10892544	157.0 ± 20.4	108.5 ± 11.2	79.6 ± 7.0	61.7 ± 5.1	49.5 ± 3.3	42.7 ± 2.3	39.8 ± 1.9	43.0 ± 2.4	49.1 ± 3.1	61.4 ± 4.8	81.9 ± 7.2
HD 205674	15022592	162.3 ± 21.3	110.1 ± 11.7	80.6 ± 7.1	61.0 ± 6.2	47.5 ± 4.0	37.4 ± 3.6	32.9 ± 2.8	31.0 ± 1.3	30.4 ± 1.8	34.5 ± 2.6	39.9 ± 2.7
HD 206893	10893056	277.5 ± 36.2	188.5 ± 20.8	135.6 ± 13.0	102.9 ± 8.6	80.2 ± 5.9	63.3 ± 4.9	51.7 ± 5.3	42.7 ± 2.0	38.2 ± 1.3	38.0 ± 0.9	42.2 ± 2.4
HD 213429	15017984	575.4 ± 84.9	391.4 ± 42.8	284.5 ± 23.8	218.8 ± 18.7	166.9 ± 13.2	130.1 ± 11.4	105.0 ± 9.3	78.4 ± 5.7	61.6 ± 5.5	48.7 ± 4.5	38.3 ± 4.9
HD 213617	10893568	285.9 ± 38.2	191.0 ± 21.0	137.9 ± 12.8	102.9 ± 8.3	80.9 ± 5.0	66.6 ± 5.4	53.2 ± 4.2	43.8 ± 2.2	38.2 ± 1.3	36.5 ± 1.3	36.3 ± 3.4
HD 221853	10894592	128.5 ± 18.0	87.1 ± 9.9	63.3 ± 4.9	53.5 ± 3.3	48.4 ± 1.3	50.9 ± 3.0	64.3 ± 8.8	92.9 ± 9.8	119.6 ± 8.7	140.1 ± 6.3	170.9 ± 12.2

Notes. Column 1: identification. Column 2: AOR Key for IRS measurement. Columns 3–13: synthetic photometry. IRS data points are averaged in 11 adjacent bins. We used 2 μm wide bins at λ < 20 μm and 3 μm wide bins at λ > 20. The quoted uncertainties include both the instrumental noise and the variation of the SED within a bin.
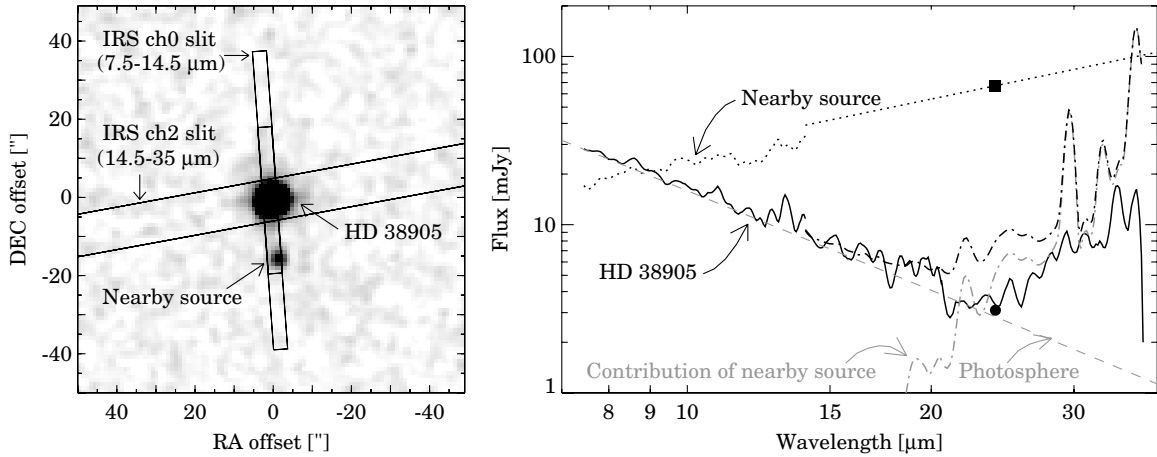
Figure 6. Left: 2MASS K_s image of HD 38905 and its surroundings. The position of the two *Spitzer*/IRS slits are overplotted. A nearby source at a distance of 13″5 is included in the ch0 slit. At these wavelengths, the two sources are well resolved and a separate spectrum for each source can be extracted. The ch2 slit is nearly perpendicular to the ch0 slit, but due to the longer wavelength, the PSF is wider, thus the nearby source might have a contribution to the ch2 spectrum extracted for HD 38905. Right: the solid black line indicates the spectrum extracted at the position of HD 38905, and the black dot is a MIPS 24 μm photometric point for HD 38905. The black dotted line indicates the spectrum of the nearby source: for $\lambda < 14.5 \mu$m, it is observed and resolved by IRS, and the black square is also a resolved MIPS 24 μm photometric point. The straight line above 14.5 μm is a linear extrapolation. Using the IRS beam profiles and the spectrum of the nearby source, we estimated the contribution this source has in the ch2 slit (gray dash-dotted line). The gray dashed line represents the stellar photosphere of HD 38905. The black dash-dotted line is the sum of the photosphere and the contribution of the nearby source. Our conclusion is that the excess emission with respect to the stellar photosphere observed at the position of HD 38905 can be well explained by the contamination from the nearby source. The shape of the nearby source's spectrum ($F_\nu \sim \lambda$) indicates that it is probably a background galaxy (see, e.g., Wu et al. 2009 or Buchanan et al. 2006). A similar analysis was done for HD 34739, HD 145371, and HD 184169, although in those cases, no resolved spectroscopy is available for the nearby sources. Supposing that these sources are also background galaxies, a spectral shape of $F_\nu \sim \lambda$ is assumed and absolute brightness level was scaled to resolved 24 μm MIPS photometry. Our analysis indicates that apart from these four stars, no other targets have suffered contamination by nearby sources.

measured with the IRAF task *splot*. The projected rotational velocity of the targets was determined via fitting theoretical models (Munari et al. 2005) to the observed spectra with the χ^2 method. Table 4 summarizes the derived properties of the observed stars.

4. RESULTS

4.1. Identification of Stars with Infrared Excess

We used our *Spitzer* data to identify stars exhibiting excess at infrared wavelengths. First, the predicted photospheric flux densities were determined at the relevant wavelengths using the best-fit Kurucz models of the stars (see Section 2.1). The average accuracy of the predicted far-infrared fluxes is estimated to be around 3%. The predicted flux densities of the stars for the MIPS bands (P_{24}, P_{70}, P_{160}) are listed in Table 2. The significance level of the infrared excess was calculated in each photometric band using the following formula:

$$\chi_\nu = \frac{F_\nu - P_\nu}{\sigma_\nu^{\text{tot}}}, \qquad (1)$$

where F_ν is the measured flux density, P_ν is the predicted stellar flux, while σ_ν^{tot} is the quadratic sum of the uncertainty of the measured flux density and the uncertainty of the predicted flux density in the specific band. When χ_ν was greater than 3 in any of the MIPS bands, the object was selected as a star with excess emission. Applying this criterion, we identified 28 stars that exhibit IR excess. One of our targets, HD 199391, shows excess only at 160 μm. Since at this wavelength the position measured on the 24 μm image was adopted in the course of photometry, we cannot exclude the possibility that the excess emission is related to a nearby background source. Thus, HD 199391 was excluded from the list of stars with excess emission. Future observations with higher spatial resolution in far-infrared

bands should reveal the true nature of the excess emission observed toward this object. Among the 27 remaining systems 15 show excess at 24 μm, all 27 exhibit excess at 70 μm, and we found excess at 160 μm in 17 cases. All of our targets that exhibit excess at 24 μm also show excess at 70 μm as well.

Although in most cases the shape of the obtained IRS spectra could be well fitted by the photospheric model of the specific target, 32 among the 82 spectra showed significant deviations. Out of the 27 objects where excess was indicated by the MIPS photometry, 25 also showed excess in the IRS spectra. In the case of HD 15060 and HD 213429, the IRS spectra were consistent with the predicted photospheric emission and these two objects showed excess only at 70 μm. Seven additional excess sources were revealed by the IRS data. In three of the seven cases (HD 143840, HD 185053, and HD 218980) the MIPS images show bright nebulosity around the stars with a spatial extent of 50″–60″ (see also Section 3.1.2). At the distance of these stars the estimated angular extents correspond to a size of 4000–7000 AU. Thus, in these cases the observed emission is likely to be of interstellar, rather than circumstellar origin. The remaining four stars (HD 34739, HD 38905, HD 145371, and HD 184169) are located close to background sources that are brighter at mid- and far-IR wavelengths than the original target. In these cases we investigated—using the beam profiles of the different IRS modules and the known position of the background sources (derived on the MIPS images)—the possibility that the observed excess emission was associated with these bright nearby objects. We found that in all four cases the apparent excess is likely to be related to the nearby sources (Figure 6 demonstrates the main steps of our analysis for HD 38905). As a consequence, these additional seven candidates were discarded from the further analysis.

A significant fraction of our candidates that were selected based on previous IR observations turned out to be misidentifications in the light of the new *Spitzer* data. Several earlier works

Table 6
Disk Properties

Source ID	T_{dust} [K]	R_{dust} [AU]	f_{dust} [10^{-4}]	Reduced χ^2
HD 3670	53 ± 1	42 ± 9	5.4 ± 0.4	0.9
HD 15060	< 64	>51	~0.16	...
HD 15115*	61 ± 1	36 ± 1	5.1 ± 0.2	3.4
HD 15745*	89 ± 1	18 ± 1	21.9 ± 0.8	2.3
HD 16743*	62 ± 1	47 ± 2	3.8 ± 0.2	7.6
HD 17390	48 ± 1	70 ± 3	2.1 ± 0.1	2.8
HD 24636	116 ± 5	10 ± 1	1.08 ± 0.06	0.5
HD 25570	51 ± 3	75 ± 9	0.53 ± 0.04	0.2
HD 30447*	67 ± 1	33 ± 2	9.2 ± 0.6	1.8
HD 32195	89 ± 9	12 ± 3	0.65 ± 0.15	1.4
HD 33081	55 ± 4	45 ± 7	0.46 ± 0.07	0.7
HD 35114	97 ± 9	12 ± 2	0.53 ± 0.07	0.4
HD 35841	69 ± 1	23 ± 5	15.2 ± 1.0	1.4
HD 36968	58 ± 1	45 ± 9	13.4 ± 1.0	1.5
HD 50571	45 ± 2	66 ± 5	1.5 ± 0.1	0.2
HD 113337	53 ± 1	55 ± 3	0.98 ± 0.07	0.5
HD 120160	57 ± 4	84 ± 14	0.81 ± 0.20	0.2
HD 125451	63 ± 5	37 ± 6	0.18 ± 0.02	0.2
HD 127821	45 ± 1	66 ± 3	2.1 ± 0.1	1.3
HD 151044	57 ± 2	32 ± 2	0.77 ± 0.05	0.7
HD 170773	43 ± 1	78 ± 3	4.8 ± 0.2	1.3
HD 192758*	61 ± 1	45 ± 9	5.7 ± 0.3	3.7
HD 205674	54 ± 1	46 ± 3	3.7 ± 0.3	2.4
HD 206893	49 ± 1	49 ± 2	2.5 ± 0.1	1.7
HD 213429	< 62	>27	~0.08	...
HD 213617	55 ± 1	59 ± 3	0.96 ± 0.05	0.7
HD 221853	84 ± 1	23 ± 1	7.9 ± 0.4	1.6

Notes. Disk parameters, listed in this table, come from a model assuming a single narrow dust ring. Disks marked by asterisks can be better fitted with a two-component model (see Table 7). Column 1: identification. Disks discovered in this program are in boldface. Column 2: disk temperature. Column 3: disk radius. Column 4: fractional dust luminosity $f_{dust} = \frac{L_{dust}}{L_{bol}}$. Column 5: best-reduced χ^2.

showed that *IRAS*-based debris candidate lists are strongly contaminated by false identifications (bogus debris disks) especially due to the low spatial resolution of *IRAS* observations at far-IR wavelengths (Kalas et al. 2002; Moór et al. 2006; Rhee et al. 2007). The most common reasons of the misidentification are (1) confusion with background sources, where the IR emission is associated with a nearby object; (2) the presence of extended nebulosity, where the IR emission is of interstellar rather than of circumstellar origin; and (3) erroneous infrared photometric measurements. The last reason played an especially important role in the case of warm disk candidates.

In total 27 stars have been identified where the observed excess emission may originate from circumstellar dust grains (see Table 5). Nine out of the 27 stars exhibiting IR excess are new discoveries (marked in Table 6).

4.2. Spectral Features in the IRS Spectra

No prominent features have been identified in the IRS spectra of the 27 stars with excess emission. This finding is consistent with the results of previous IRS observations related to debris disks around solar-like and more massive A-type stars: although many debris systems show significant excess in the wavelength range between 5 and 35 μm the majority of these systems do not possess spectral features (Chen et al. 2006; Carpenter et al. 2009b; Lawler et al. 2009; Morales et al. 2009).
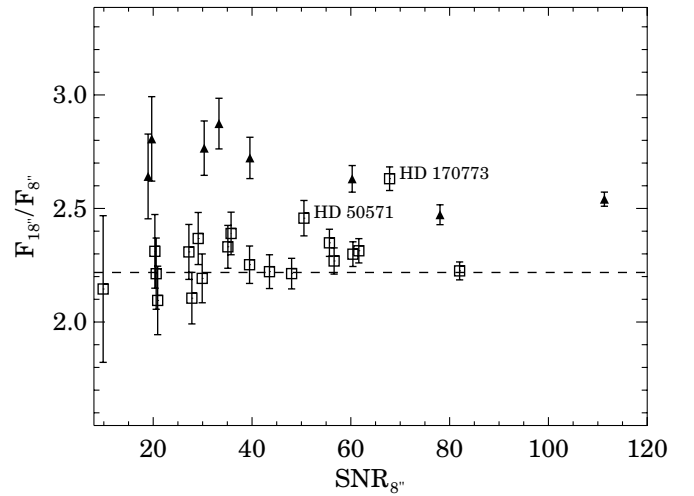
Figure 7. Ratio of the flux density measured in apertures with radii of 18″ and 8″ as a function of the SNR obtained in the smaller aperture. Squares indicate our stars that exhibit excess at 70 μm, triangles correspond to debris disks (HD 10647, HD 38858, HD 48682, HD 105211, HD 115617, HD 109085, HD 139664, and HD 207129) that found to be marginally resolved at this wavelength by Bryden et al. (2006).

4.3. Spatially Extended Sources at 70 μm

Observations with the MIPS detector at 70 μm revealed several (marginally) resolved debris disks even at relatively large distances from the Sun (e.g., Bryden et al. 2006; Su et al. 2009). In order to identify sources with extended emission, in Figure 7 we plotted the ratio of the flux density measured in apertures with radii of 8″ and 18″ as a function of the S/N obtained in the smaller aperture. Similar ratios derived for some known resolved debris disks (based on the list of Bryden et al. 2006) were also plotted. MIPS 70 μm data for these objects were downloaded from the *Spitzer* Archive and processed using the same method applied to our targets. As expected, objects with known extended disks show significantly larger flux ratios. Utilizing the *Spitzer* TinyTim software (Krist 2002) and applying the smoothing procedure proposed by Gordon et al. (2007), we calculated the PSF of a 60 K blackbody source that was used to derive the expected flux ratio plotted in Figure 7. By comparing the obtained flux ratios to the expected one, we found that two of our sources—HD 50571 and HD 170773—show significant (>3σ level) deviation and may be spatially extended at 70 μm. In order to model the observed profiles, we convolved the PSF with different Gaussian profiles. The minor- and major-axis FWHMs as well as the position angle of the major axis of the Gaussians were varied to find the best-fitting model profile. We found that the measured profile for HD 50571 can be well fitted using a Gaussian broadened by 9.″5 only in one direction along a position angle of 91° (measured from north to east). In the case of HD 170773, a convolution by a Gaussian with minor- and major-axis FWHMs of 9″ and 10″ with position angle of 110° provided the best fit. MIPS 70 μm photometry for these sources, which takes into account the spatial extent, is given in Table 2.

It is a common expectation that the rotational spin axis of the star is aligned with the orbital spin axis of the planetesimals. HD 50571 has an unusually high projected rotational velocity of 60 km s^{-1} (Holmberg et al. 2007). When comparing this value to the $v \sin i$ of 1566 stars with similar effective temperatures ($T_{eff} = 6480 \pm 100$ K) included in the same catalog (Holmberg et al. 2007), we found that the projected velocity of HD 50571

is higher than 99.4% of that of the catalog sample. This implies a very high inclination of the spin axis and consistent with our finding that the disk around this star may be seen nearly edge-on (it is resolved only in one direction). The derived size of the debris disk around HD 170773 indicates that it might be seen close to pole-on. It is interesting that the projected rotational velocity is remarkably high (see Table 4) for this orientation.

4.4. Modeling the Observed Infrared Excess

The infrared excess emission of F-type main-sequence stars is generally believed to be attributed to the optically thin thermal emission of second-generation circumstellar dust grains heated by the central star. Since no resolved images are available for our targets, the fundamental parameters of these dust disks have to be derived by modeling the SEDs of the systems. Four newly discovered disks have already been modeled in a previous paper (Moór et al. 2009). For the remaining 27 stars exhibiting excess emission, we compiled the SED from the data listed in Section 3. For the fitting process the IRS spectra were sampled in 11 adjacent bins (for the center and width of the bins as well as for the obtained flux densities see Table 5). We used a simple model to characterize the disk properties based on the excess emission. We assume that the dust grains are distributed around a single radius and we adopt the same temperature for all particles within this ring. Then the excesses are fitted by a single temperature modified blackbody, where the emissivity is equal to 1 at $\lambda \leqslant \lambda_0$ and vary as $(\lambda/\lambda_0)^{-\beta}$ at $\lambda > \lambda_0$ wavelengths. We used this modified blackbody model in order to account for the falloff in the emission spectrum at longer wavelengths, that is faster than in the case of a blackbody. Following Williams & Andrews (2006) we fixed λ_0 to 100 μm consistent with the lack of spectral features in the IRS spectra which indicates a relatively large average grain size. Since β cannot be reliably determined in all systems due to the lack of long wavelength data, we decided to estimate a characteristic β value based on those disks where the excess emission at $\lambda > 50\,\mu$m was measured with $\chi_\nu > 3$ in at least four different bands and were successfully detected at $\lambda > 100\,\mu$m as well. A Levenberg–Marquardt algorithm was used to fit the model to the measured data and an iterative method was used to compute and apply color corrections for the photometric data during the fitting process (see, e.g., Moór et al. 2006). Figure 8 shows the obtained β parameters for the selected 11 disks. A characteristic β value of 0.7, derived by computing the weighted average of these values, seems to represent very well the whole sample. Thus, in the following we fixed β equal to 0.7 and λ_0 to 100 μm and repeated the fitting process for all debris systems. In two cases when the excess was detected only in the MIPS 70 μm band, we determined the highest possible dust temperature which was still consistent with the IRS data. The derived dust temperatures ($T_{\rm dust}$) and the reduced chi-square values of the best fits are quoted in Table 6. We note that using a simple blackbody model instead of the modified blackbody would change the dust temperatures less than their formal uncertainties, but would yield worse fitting for the long wavelength data in most cases when we have $\lambda > 100\,\mu$m measurements.

Most of our SEDs can be fitted well using the simple model described above. However, in several cases systematic deviations between the model and measured fluxes can be seen, especially at shorter wavelengths, where the model typically underestimates the observed excess. For example, for HD 16743 and HD 192758 the high reduced chi-square values indicate poor model fit. It is a general trend among the deviating cases
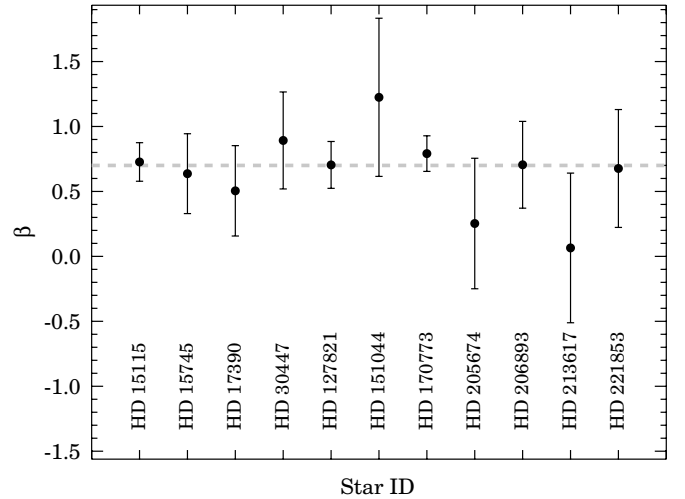
Figure 8. Derived β values for some selected disks (see Section 4.4).

that fitting only the IRS spectra yields higher dust temperature estimates than fits based on the long wavelength photometric points. We also found that the extrapolation of IRS-based fits to longer wavelengths underpredicts the excess measured in the *IRAS*, ISOPHOT, and MIPS bands. Several authors reported similar findings in different debris disk samples (Hillenbrand et al. 2008; Carpenter et al. 2009b; Morales et al. 2009). One possible explanation for the observed discrepancy is that dust grains in these systems are distributed in two spatially separated rings similarly to our Solar System, where the majority of dust grains are thought to be co-located with the main asteroid and with the Kuiper Belt. Assuming that the dust is concentrated in two distinct narrow rings, we used a two-component model, where grains in the warmer component act like blackbodies, while the emission of the outer ring can be described by the modified blackbody as defined above. To decide whether a single or a two-component model should be used for a certain target, we used a variant of the Akaike Information Criterion, the so-called AICu, proposed by McQuarrie & Tsai (1998). The value of AICu can be calculated as

$$\mathrm{AICu} = \ln\frac{\mathrm{SSE}_k}{n-k} + \frac{2(k+1)}{n-k-2}, \qquad (2)$$

where n is the number of observations, k is the number of parameters in the model, while SSE_k is the usual sum of squared errors. Besides the fact that the Akaike Information Criterion take into account the goodness of fit, it penalizes the usage of unnecessary additional model parameters. This test can be used to rank the competing models, from which the best one gives the lowest AICu value. We found the two-component model to be better in five cases (HD 15115, HD 15745, HD 16743, HD 30447, and HD 192758). The derived parameters of these five disks are presented in Table 7. The SED and the best-fit models for each of our targets are plotted in Figure 9.

The fractional luminosity of the disks was computed as $f_{\rm dust} = L_{\rm dust}/L_{\rm bol}$. The integrated dust emission was derived based on the fitted model while the star's luminosity was calculated from the best-fit Kurucz model. We estimated the radius of the dust ring (or rings) using the following formula (Backman & Paresce 1993):

$$\frac{R_{\rm dust}}{\mathrm{AU}} = \left(\frac{L_{\rm star}}{L_\odot}\right)^{0.5}\left(\frac{278\,\mathrm{K}}{T_{\rm dust}}\right)^2. \qquad (3)$$
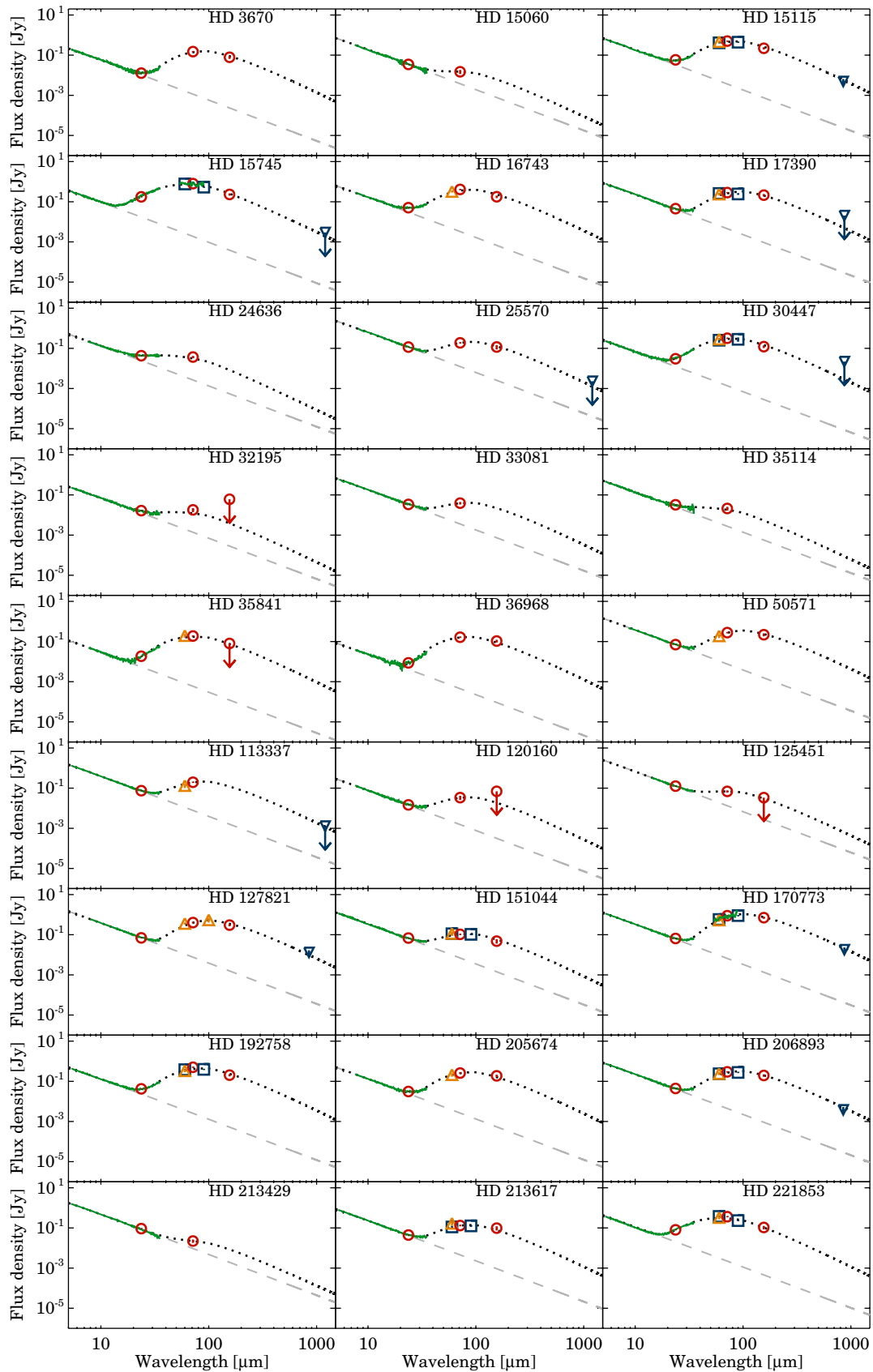
Figure 9. Spectral energy distributions (SEDs) for stars exhibiting IR excess in our sample. The different symbols represent the following photometric data—circles (red in online version): MIPS, squares (blue in online version): ISOPHOT, triangles (red in online version): *IRAS*, upside down triangles (blue in online version): submillimeter/millimeter observations. The IRS and MIPS SED spectra are displayed with solid lines (solid green lines in online version). The photospheric models and the disk models are shown by dashed gray lines and dotted black lines, respectively. For HD 15115, HD 15745, HD 16743, HD 30447, and HD 192758 the two-component disk models are displayed.

(A color version of this figure is available in the online journal.)

15

Table 7
Disk Properties

Source ID	Warm Dust			Cold Dust			Reduced χ^2
	$T_{\rm dust}$ [K]	$R_{\rm dust}$ [AU]	$f_{\rm dust}$ [10^{-4}]	$T_{\rm dust}$ [K]	$R_{\rm dust}$ [AU]	$f_{\rm dust}$ [10^{-4}]	
HD 15115	179 ± 46	4 ± 2	0.38 ± 0.08	57 ± 1	42 ± 2	4.8 ± 0.2	1.6
HD 15745	147 ± 22	6 ± 2	3.5 ± 1.6	81 ± 3	21 ± 2	18.9 ± 2.0	1.1
HD 16743	147 ± 24	8 ± 3	0.51 ± 0.07	53 ± 1	63 ± 4	3.6 ± 0.3	1.7
HD 30447	159 ± 36	6 ± 3	0.66 ± 0.32	62 ± 2	38 ± 3	8.8 ± 0.7	0.8
HD 192758	154 ± 31	7 ± 3	0.39 ± 0.09	56 ± 1	53 ± 11	5.4 ± 0.3	1.8

Notes. Column 1: identification. Column 2: temperature of warm dust in the inner ring. Column 3: radius of the inner dust ring. Column 4: fractional dust luminosity of the inner dust ring. Column 5: temperature of cold dust in the outer ring. Column 6: radius of the outer dust ring. Column 7: fractional dust luminosity of the outer dust ring. Column 8: best-reduced χ^2.

Because this formula assumes blackbody-like grains, the resulting $R_{\rm dust}$ corresponds to a minimum possible radius. The obtained fundamental disk properties are listed in Tables 6 and 7.

We made several simplifying assumptions in the applied model. Collisions among planetesimals in debris disks produce a collisional cascade, in which collisions gradually grind large bodies into smaller ones that are removed by radiation forces. This process is thought to result in a characteristic dust grain size distribution and copious amounts of small dust (Wyatt 2008, and references therein). Even if planetesimals are distributed in a narrow ring, the radiation pressure pushes the smallest grains into more eccentric orbits extending the dust disk outward. Moreover, the planetesimal ring(s) can be extended. Our model assumes relatively large grains that act like a blackbody at $\lambda \leqslant 100\,\mu{\rm m}$ located in one (or two, see above) ring(s) of dust. Both the existence of smaller dust grains—that are ineffective emitters and therefore have higher temperature than large grains at the same radial distant from the star—and the finite radial extension lead to multi-temperature distribution.

Two of the multiple temperature disks from Table 7 were resolved or marginally resolved in scattered light. Note, however, that different observation techniques are sensitive to different populations of dust grains. The scattered light images are expected to trace very small grains which may show different spatial distribution than those grains which dominate the mid- and far-IR emission of the disk (Wyatt 2006), because a significant fraction of small grains could be blown out from the system outside the planetesimal ring. Using coronagraphic images, Kalas et al. (2007b) and Debes et al. (2008) successfully resolved a very extended circumstellar disk around HD 15115 at optical and near-IR wavelengths, revealing a strongly asymmetric disk structure. The lobes of the disk can be traced inward to ∼31 AU. It could be consistent both with our single/two-ring models where the outer ring is located at ∼40 AU. HD 15745 was also resolved in scattered light using the Advanced Camera for Surveys aboard the *Hubble Space Telescope* (Kalas et al. 2007a). The circumstellar disk is detected between ∼128 and 480 AU radius. The detection at the inner part of the disk is limited by PSF subtraction artifacts, thus this image does not provide further information about the disk morphology in the inner regions. Our model with an outer ring at 21 AU disk is not inconsistent with this result. Since the existing data do not allow to localize the warm dust unambiguously, in the following analysis of the five disks in Table 7, we assume that the warm emission originates from an inner ring.

Two additional disks in our sample were marginally resolved in the 70 μm images (Section 4.3). The measured broadening suggests a dust structure size of 320 AU and 370 AU for

HD 50571 and HD 170773, respectively. Although both stars harbor relatively cold and extended dust rings, the minimum diameters of 132 AU and 146 AU, derived from our simple model, are significantly lower than the measured extensions. One possible explanation would be a dust structure similar to that of the F5/F6V star HD 181327 (not included in our sample), where Schneider et al. (2006) discovered a dust ring using NICMOS coronagraphic observations. The extension of this ring (∼86 AU) significantly exceeds the modeled dust radius of 22 AU derived from the SED of the object assuming blackbody grains (Schneider et al. 2006). They propose that a large amount of small dust particles in the ring can explain the observed discrepancy since small grains are hotter than large grains at the same location. An analogy with Vega can provide another explanation. Using MIPS observations that resolved the source, Su et al. (2005) found that the radius of the disk at 70 μm exceeds significantly the size of the disk seen at submillimeter wavelengths. The discrepancy probably comes from an extended cloud of small particles blown away from a planetesimal ring by the radiation pressure of the star. Due to the marginal resolution of the *Spitzer* 70 μm observations of HD 50571 and HD 170773, we cannot decide between the two scenarios. In the further analysis of these two objects we adopt the parameters listed in Table 6.

Using the derived disk parameters in Tables 6 and 7, we estimated both the PR ($\tau_{\rm PR}$) and the collision timescales ($\tau_{\rm coll}$) for grains with radii ranging between the grain size corresponding to the blowout limit and 1000 μm. The blowout limit was computed using the equation presented by Hillenbrand et al. (2008):

$$a_{\rm blow} = 0.52 \frac{2.5\,{\rm g\,cm^{-3}}}{\rho} \frac{L_*/L_\odot}{(T_*/5780)}, \qquad (4)$$

where ρ is the density of the grain (assumed to be 2.7 g cm^{-3}). The PR timescales were estimated based on Equation (14) in Backman & Paresce (1993), while the collisional timescales were computed using the semiempirical formulae (Equations (7)– (8)) derived by Thébault & Augereau (2007). We found that for our disks $\tau_{\rm coll} \ll \tau_{\rm PR}$ for all grain sizes and the obtained timescales are short with respect to the ages of the stars, implying that the grains have second-generation ("debris") nature and their evolution is mainly governed by collisions.

In a debris disk the mutual collisions continually grind down the larger planetesimals into smaller fragments that can be removed by the PR drag and by the radiation pressure. Since the estimated collisional timescale in our disks is significantly shorter than the PR-drag lifetime, the dust removal processes in these systems may be collisionally dominated. In such a disk, the frequent collisions shatter dust grains more rapidly to

Table 8
Age Estimates

Source ID	$\log \frac{L_x}{L_{bol}}$	$\log R'_{HK}$	Ref.	Membership	Ref.	Age [Myr]	Dating Method	Ref.
HD 3670	−4.39	...	...	Columba assoc.	1	30	1	...
HD 15060	...	...	...	...	...	2300 ± 100	6	1
HD 15115	−4.93	...	...	β Pic mg.	3, 4	12	1	...
HD 15745	...	...	...	β Pic mg.	1	12	1	...
HD 16743	...	...	...	...	...	10–50	2, 3, 5	...
HD 17390	−5.15	...	...	...	...	1000^{+300}_{-400}	6	1
HD 24636	−5.41	...	...	Tucana-Horologium assoc.	1	30	1	...
HD 25570	−5.24	...	...	Hyades?	see Section 4.5	625 ± 50	1	...
HD 30447	...	...	...	Columba assoc.	3, 4	30	1	...
HD 32195	−3.92	...	...	Tucana-Horologium assoc.	4, 5	30	1	...
HD 33081	...	...	...	...	...	3100^{+400}_{-500}	6	1
HD 35114	−3.86*	...	...	Columba assoc.	4	30	1	...
HD 35841	...	...	...	Columba assoc.	3, 4	30	1	...
HD 36968	...	...	...	Octans assoc.	1	20	1	...
HD 50571	−5.27	−4.55	1	B3 group	1	300 ± 120	1, 6	3
HD 113337	−5.07*	...	...	...	...	40 ± 20	2	...
HD 120160	...	...	...	...	...	1300 ± 100	6	1
HD 125451	−5.10	−4.37	3	Ursa Major mg.	2	500 ± 100	1	...
HD 127821	−5.11	...	...	...	...	220 ± 50	6	2
HD 151044	...	−5.0	4	...	...	3000^{+1300}_{-1000}	2, 3	...
HD 170773	−4.98*	−4.39	1	...	...	200	6	3
HD 192758	...	...	...	Argus assoc.	3	40	1	...
HD 205674	−5.13	...	...	ABDor mg.?	...	70–300	1, 6	3
HD 206893	−4.87*	−4.47	1	...	...	200^{+1000}_{-200}	6	1, 3
HD 213429	...	−4.83	2	...	...	2200^{+1300}_{-800}	3, 6	1
HD 213617	...	...	...	...	...	1200 ± 300	6	1
HD 221853	...	...	...	Local Association	3	20–150	1	...

Notes. Column 1: identification. Column 2: fractional X-ray luminosity based on *ROSAT* data. Asterisks indicate those objects where the correlation between the X-ray source and the star is confirmed by observations with the *XMM* satellite (*XMM-Newton* slew survey Source Catalogue; Saxton et al. 2008) as well. Column 3: fractional Ca II H&K luminosity ($\log R'_{HK}$). Column 4: references for $\log R'_{HK}$ data: (1) Gray et al. (2006), (2) Gray et al. (2003); (3) King & Schuler (2005); (4) Wright et al. (2004). Column 5: membership status of the star. Column 6: references for the identification of star as a member of a specific kinematic group in Column 5: (1) this work; (2) King et al. (2003); (3) Moór et al. (2006); (4) Torres et al. (2008); (5) Zuckerman & Song (2004b). Column 7: estimated age of the star and its formal uncertainty. Column 8: used age-dating methods: (1) stellar kinematic group or cluster membership; (2) isochrone fitting; (3) diagnostic of chromospheric activity indicator; (4) diagnostic of coronal activity indicator; (5) lithium abundance; (6) literature data. Column 9: references for the literature data mentioned in Columns 7–8: (1) Holmberg et al. (2009); (2) A. Moór et al. 2011b, in preparation; (3) Rhee et al. (2007).

sizes below the blowout limit before the effect of the PR drag can be manifested. Due to the stellar radiation pressure, grains smaller than the blowout limit are ejected on a short timescale, while somewhat larger grains are pushed into a more eccentric orbit. Thus, in a collisionally dominated disk, the dust grains extend outward from their birth ring, where the planetesimals are located. However, since the lifetime of blowout grains is significantly shorter than the normal grains' lifetime, it is a plausible assumption that the dominant part of the dust mass is co-located with the parent planetesimals. Thus, in the further analysis we assume that the derived radii of the dust rings can be considered as the size of the underlying planetesimal belts as well.

4.5. Age Determination

In order to estimate the age of the 27 debris systems, we use the following general strategy. The most accurate and reliable dating can be derived via cluster membership. Thus, if a specific target can be assigned to a stellar kinematic group then we adopt the age of the group for the star. Beside the nine previously known cluster members, we classify five new young moving group members among our targets (for more details related to the new assignments see below). For field stars, isochrone fitting combined with diagnostics of rotation-driven activity indicators and lithium content (especially that of

late-type companions) are considered in the age estimates. In the analysis of chromospheric and coronal activity indicators, the calibration derived by Mamajek & Hillenbrand (2008) is applied whenever it was applicable (i.e., the $B − V$ color indices fall in the appropriate range). In the case of lithium content, our age estimates are based on comparisons with the distribution of similar properties in well-dated open clusters (Sestito & Randich 2005) and young moving groups (Mentuch et al. 2008; da Silva et al. 2009). Pre-main-sequence evolutionary models are used if the lithium content or the activity indicators measured in the target or in its late-type companion indicated that the specific system may be in a pre-main-sequence evolutionary stage. We use literature data for several stars. Among the 27 debris systems, 13 are younger than 100 Myr. Table 8 summarizes the age-related data for stars with debris disks.

HD 3670. The derived galactic velocity components of HD 3670, $U = −12.6$, $V = −22.6$, $W = −4.6$ km s^{-1}, are consistent with the characteristic motion of the 30 Myr old Columba association (see Torres et al. 2008). HD 3670 has a *ROSAT* counterpart with fractional X-ray luminosity of $\log(L_x/L_{bol}) = −4.39$, which is comparable with the fractional X-ray luminosity of those stars with similar spectral type in the Columba association and supports the youthfulness of the star.

HD 15745. Based on our new radial velocity measurements (Table 4), we recomputed the galactic space velocities of this
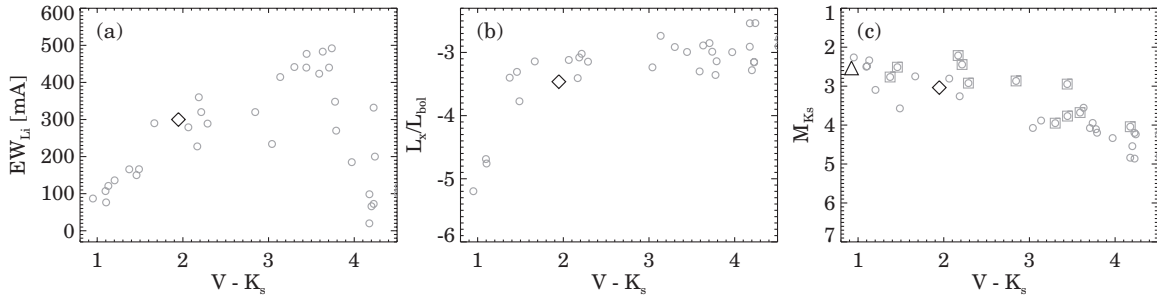
Figure 10. (a) The distribution of Li equivalent widths as a function of $V − K_s$ color indices. (b) The distribution of fractional X-ray luminosities as a function of $V − K_s$ color indices. (c) Color–magnitude diagram. Gray circles represent the known members of the β Pic moving group. Gray squares represent binary stars in the CMD. The black diamond represents BD+45° 598, the black triangle shows HD 15745.

star, obtaining $−10.4$, $−15.3$, $−7.9$ km s^{-1} for the U, V, W components, respectively. This space velocity corresponds well to the characteristic space motion of the β Pic moving group (see Torres et al. 2008).

In the framework of a recent high-resolution spectroscopic survey focusing on optical counterparts of X-ray sources, Guillout et al. (2009) discovered several new post-T Tauri stars located on the northern hemisphere. One of them, BD+45° 598—which is offset by $\sim 9°$ from HD 15745—shows very similar proper motion and radial velocity ($\mu_{\alpha\cos\delta} = 44.7 \pm 1.1$ mas, $\mu_\delta = −44.3 \pm 1.0$ mas, $v_r = −0.77 \pm 0.97$ km s^{-1}) to that of our target ($\mu_{\alpha\cos\delta} = 45.8 \pm 0.6$ mas, $\mu_\delta = −47.9 \pm 0.5$ mas, $v_r = +2.5 \pm 3.3$ km s^{-1}). BD+45° 598 was classified as a K1-type star by Guillout et al. (2009). The measured lithium equivalent width and the fractional X-ray luminosity of this star are consistent with the similar properties of the known β Pic members (see Figures 10(a) and (b)). Assuming that BD+45° 598 also belongs to the β Pic moving group, a kinematic distance of 70 pc can be estimated for it, obtaining $−10.4$, $−16.2$, and $−8.1$ km s^{-1} as its galactic space motion. The position of the two stars on the color–magnitude diagram of the β Pic moving group also confirms their membership status (see Figure 10(c)). The fact that HD 15745 harbors a debris disk with very large fractional dust luminosity also supports this assignment.

Therefore, we propose that both HD 15745 and BD+45° 598 are new members of the β Pic moving group and we adopt an age of 12 Myr for HD 15745.

HD 16743. Both the proper motion ($\mu_{\alpha\cos\delta} = 73.12 \pm 0.27$ mas, $\mu_\delta = 49.65 \pm 0.3$ mas) and the trigonometric parallax ($\pi = 16.99 \pm 0.31$ mas) of HD 16743 are in good agreement with the corresponding astrometric properties of HD 16699AB ($\mu_{\alpha\cos\delta} = 72.33 \pm 0.86$ mas, $\mu_\delta = 48.56 \pm 0.87$ mas, and $\pi = 16.54 \pm 0.99$ mas), that is also a multiple system itself with a separation of 8″.7 (HD 16699+SAO 232842). The similarities of the measured radial velocities of the three stars (see Table 4) also confirm that they may form a wide multiple system. This offers a good opportunity to improve the age determination of HD 16743 by combining the result of different age diagnostic methods for the three members of the system.

The *ROSAT* source J023845.4−525710 is located close to both HD 16699 (with separation of 12″.6) and SAO 232842 (3″.9). This X-ray source is also present in the *XMM-Newton* slew survey Source Catalogue (XMMSL1 J023845.1−525708; Saxton et al. 2008), located 1″ away from the position of SAO 232842. Due to the better positional accuracy of the *XMM* catalog, the latter data make it clear that the X-ray source corresponds to SAO 232842. The high fractional X-ray luminosity of the source, $L_x/L_{bol} = −3.32$, is comparable with that of stars with similar spectral type in the Pleiades and in
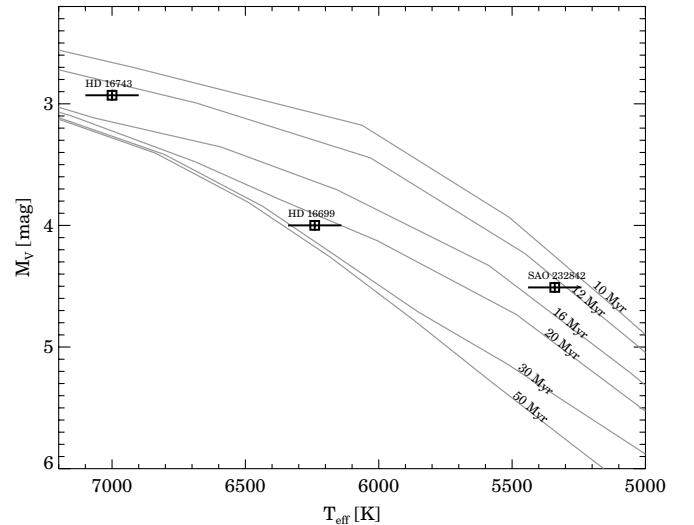
Figure 11. H-R diagram for the HD 16743 system overplotted by isochrones for different ages between 10 Myr and 100 Myr. The isochrones are taken from Siess et al. (2000). The effective temperature of HD 16699 and SAO 232842 was estimated using the same method as described in Section 2.1.

young nearby moving groups confirming a young age for this object.

The age estimates based on the lithium abundance measured in HD 16699 and SAO 232842 are somewhat controversial. The high lithium abundance in SAO 232842 suggests a very young age, it exceeds the upper envelope of the distribution of lithium equivalent width measured in Pleiades stars and consistent with the lithium content of late-type G stars belonging to very young (<40 Myr old) stellar kinematic groups and open clusters. On the other hand, the lithium equivalent width measured in HD 16699 suggests an older age, since it is somewhat lower than for stars with comparable effective temperatures in the Hyades and Coma Berenice open clusters (age $\sim$ 500–600 Myr).

Figure 11 shows the positions of the three components in the H-R diagram overplotted by isochrone models from Siess et al. (2000) for ages between 10 Myr and 50 Myr for a metallicity of $Z = 0.014$. Assuming, primarily based on the characteristics of SAO 232842, that the system is in a pre-main-sequence evolutionary stage, the positions of the three components suggest an age between 10 Myr and 50 Myr.

HD 16743 and HD 16699AB belong to a very wide multiple system with a minimum separation of $\sim$12,700 AU. Gravitational perturbations due to the subsequent encounters with other stars and giant molecular clouds during the galactic orbit would detach such wide binaries. Thus, the existence of this system is also an additional argument concerning the young age.
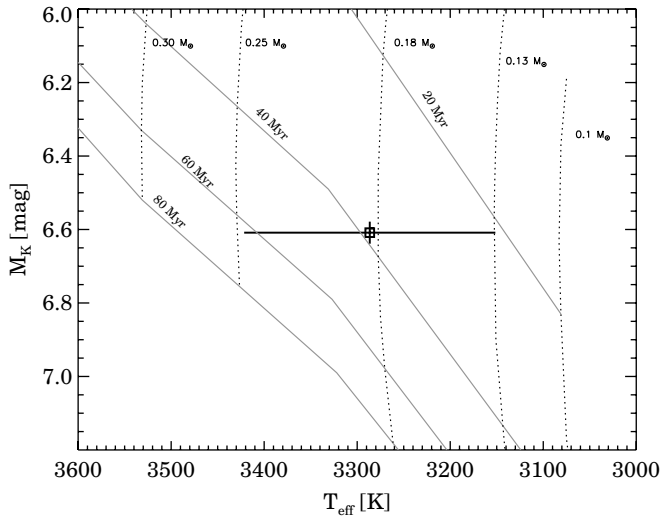
Figure 12. H-R diagram for HD 113337B. The effective temperature of the star and its uncertainty are estimated based on spectral class information (1 subclass uncertainty is assumed), the absolute magnitude in the K band is computed by assuming that it is located at the same distance as the primary component. Mass tracks and isochrones computed by Siess et al. (2000) for the evolution of stars with solar metallicity are overplotted. Based on these evolutionary tracks we find the age of the HD 113337B to be 40 ± 20 Myr and the mass is ~ 0.13–$0.25\ M_\odot$.

Figure 13. K_s–[24] color vs. the effective temperature. The square shows the position of HD 113337B, the dashed line represents the locus of stellar photospheric colors determined by Gautier et al. (2007).

Taking into account age estimates obtained from the different dating methods, we propose an age of 10–50 Myr for the HD 16743 system.

Both HD 16699 and SAO 232842 are detected and their fluxes are derived via PSF fitting on the MIPS 24 μm image of HD 16743. The obtained flux densities of 16.4 ± 0.7 mJy and 18.8 ± 0.8 mJy correspond well to the predicted photospheric flux densities in this band for both targets.

HD 24636. The derived galactic space motion of HD 24636 (see Table 4) is consistent with the characteristic space motion of the 30 Myr old Tucana-Horologium association (see Torres et al. 2008). HD 24636 is located quite close to two other Tucana-Horologium stars from our sample (HD 32195, HD 53842), and all of these objects are within a sphere 14 pc across. Interestingly, all three stars exhibit relatively warm infrared excess ($T_{\rm dust} \gtrsim$ 90 K; see Table 6 and Moór et al. 2009).

HD 25570. Eggen (1982) classified HD 25570 as a star that belongs to the Hyades group. Perryman et al. (1998) found that HD 25570 is only just outside their 3σ membership criteria and speculated that may be an example of an object just moving away from the Hyades but still close to the tidal radius. For the further analysis we consider HD 25570 as a Hyades member and adopt an age of 625 Myr for the star.

HD 36968. Both the galactic space motion ($[U, V, W]$ = $[-14.8, -6.6, -8.5]$ km s^{-1}) and the galactic position of HD 36968 ($[X, Y, Z] = [-51, -108, -73]$ pc) are consistent with those of the recently discovered $\sim$ 20 Myr old Octans Association (see Figure 17 in Torres et al. 2008). HD 36968 is the first member of this association where the existence of a debris disk was revealed by our results. The very high fractional luminosity of this debris disk is also consistent with this young age.

HD 50571. HD 50571 is an F7-type star that shows both moderate chromospheric ($R'_{\rm HK} = -4.55$; Gray et al. 2006) and coronal activity ($\log \frac{L_{\rm x}}{L_{\rm bol}} = -5.27$). Its galactic motion ($U = -16.6 \pm 0.3$, $V = -22.3 \pm 0.7$, $W = -4.4 \pm 0.3$ km s^{-1}) as well as its galactic position are consistent with those of the
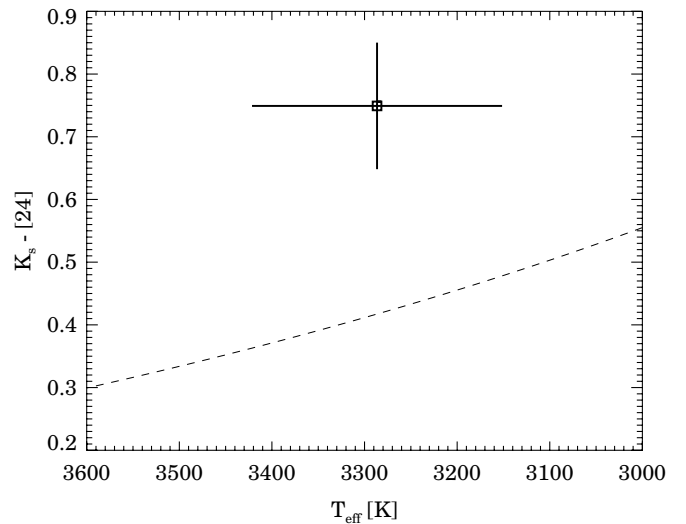
"B3" subgroup of the Local Association, implying an age of 300 ± 120 Myr (Asiain et al. 1999). Using an independent age estimating method, Rhee et al. (2007) also derived 300 Myr as the age of the object.

HD 113337. HD 113337 has a late-type companion with a separation of $\sim 120''$. The companion's proper motion ($\mu_{\alpha \cos \delta} = -174 \pm 4$ mas, $\mu_\delta = 26 \pm 1$ mas) is consistent with that of HD 113337 ($\mu_{\alpha \cos \delta} = -171.7 \pm 0.3$ mas, $\mu_\delta = 25.4 \pm 0.2$ mas). Based on medium resolution spectroscopic observations, Reid et al. (2007) classified the companion as an M3.5 dwarf with strong H_α emission ($\log \frac{f_{\rm H_\alpha}}{f_{\rm bol}} = -3.31$). The companion is also included in the 2MASS and Sloan Digital Sky Survey (SDSS) catalogs. Utilizing the spectroscopic analysis of a large number of M-type stars from the SDSS, West et al. (2008) provided characteristic median SDSS/2MASS colors ($r - i, i - z, z - J, J - H, H - K$) for different spectral subclasses (see their Table 1). Comparing the measured colors of HD 113337B with the quoted median values, we classify it as an M4-type star, confirming the result of Reid et al. (2007). Using the spectral class information, we estimated the effective temperature of the star utilizing the formula of Gray & Corbally (2009), $T_{\rm eff}[K] = 3759 - 135x$, where x is the optically defined spectral type valid for optical types M0 through L8 with $x = 0$ for an M0-type, $x = 4$ for an M4-type star, etc. Adopting 3.5 for the value of x, this equation yields ~ 3290 K as the effective temperature of HD 113337B. The age of the companion is estimated by comparing its position in the H-R diagram with the evolutionary tracks compiled by Siess et al. (2000), yielding $\sim 40 \pm 20$ Myr (see Figure 12). This age estimate is adopted for the whole system (a similar age estimate was proposed by Rhee et al. 2007).

Aperture photometry for HD 113337B on the 24 μm image yields a flux density of 2.38 ± 0.22 mJy. After a conversion of the 24 μm MIPS flux to magnitude we can compare the measured K_s − [24] color of the star to the stellar photospheric colors determined from a study of nearby M-type stars by Gautier et al. (2007). On the basis of this comparison (see Figure 13) HD 113337B shows $>3\sigma$ excess at 24 μm. The presence of circumstellar dust may explain the observed excess. However, since the significance of the excess detection is just above the

3σ level, confirmation at additional wavelengths with higher sensitivity and spatial resolution is desirable. These observations can also help to exclude alternative explanations of the apparent excess, like the possibility of contamination by a background galaxy or the presence of an unresolved low mass companion. Assuming that HD 113337B hosts a debris disk, we note that the number of known debris disks around M-type stars is very limited (Forbrich et al. 2008) and all sources in this small sample showing excess at 24 μm are younger than 50 Myr.

HD 205674. Apart from the star's galactic space velocity component toward the Galactic center, that differs from the average U velocity component of the AB Dor moving group more than 2σ, the other velocity and space components are in good agreement with the similar properties of this kinematic assemblage (see Table 1 and Figure 21 in Torres et al. 2008). HD 205674 fits well to the locus of AB Dor stars in the color–magnitude diagram. It has an X-ray counterpart as well (see Table 8). Rhee et al. (2007) proposed an age of 300 Myr. Since currently no reliable age-dating criteria for the youth of HD 205674 are available and the membership status is questionable because of the deviation of U space velocity component from the cluster center, we adopt an age range which covers both the age of the moving group (70–150 Myr; Luhman et al. 2005; Torres et al. 2008) and the 300 Myr.

5. DISCUSSION

Our investigation of 82 F-type stars with the *Spitzer Space Telescope* resulted in the detection of 27 debris disks, out of which 9 are new discoveries. In the following we analyze the parameters of these disks with special attention to disk evolution and host star properties.

5.1. Metallicity

Table 1 lists metallicity estimates for 24 out of the 27 disk bearing stars. The average metallicity value in this sample is -0.09 ± 0.09. For comparison we selected 9138 stars from the Geneva–Copenhagen Survey of Solar neighborhood (Holmberg et al. 2007) with effective temperature falling in the range spanned by our sample. Their average metallicity, -0.11 ± 0.22, is in good agreement with the result for our stars. Narrowing the comparison sample to stars with similar age range would not change the conclusion. Thus, our sample is similar to stars located in the Solar vicinity in terms of metallicity. This is in accordance with findings that the incidence of debris disks does not correlate with stellar metallicity (Beichman et al. 2006; Greaves et al. 2006). The lack of any such correlation may suggest that the formation of planetesimals is not sensitive to the metallicity in the protoplanetary disks.

5.2. Multiplicity

The effect of binarity on the presence of debris disks was studied by Trilling et al. (2007). They found that the incidence of debris disks is ~50% in systems with small (<3 AU) or wide (>50 AU) separations, even higher than the corresponding value among single systems. In our 82-star sample there are 23 known multiple systems (13 have known separation). Three of the multiple systems harbor debris disks. Two disks are associated with the widest binaries with separation >4400 AU, where the components practically can be regarded as isolated stars. It is interesting to note that in the case of HD 113337, the secondary component might also harbor a debris disk based on the 24 μm image (Section 4.5). The third disk encircles HD 213429, which
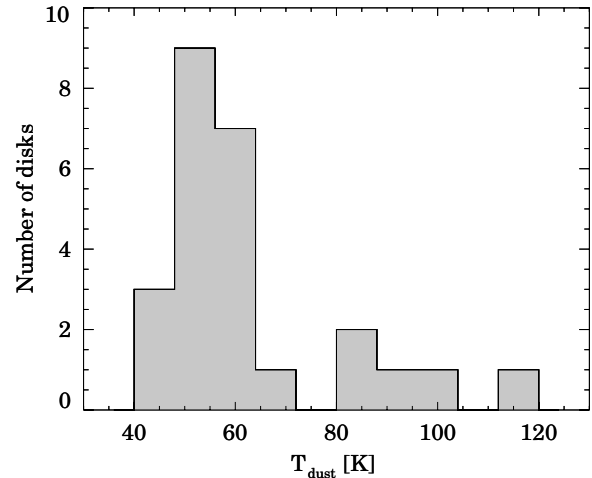
Figure 14. Histogram of the derived dust temperatures. In those cases where the presence of two separated dust rings are assumed only the temperature of the colder ring has been taken into account.

is a spectroscopic binary whose orbital solution (Pourbaix 2000) indicates the smallest known separation in our sample (1.8 AU), probably forming a circumbinary structure. Thus, all three binaries fall in groups of multiple systems where the incidence of debris disks is high according to Trilling et al. (2007).

5.3. Disk Temperature

The dust temperature provided by our modeling (Section 4.4) is a fundamental disk parameter, whose computation includes only a few assumptions and can be determined with confidence. In Figure 14, we plot a histogram of the derived dust temperature values. In those five cases when the SED was modeled by multiple dust rings (Table 7) only the colder component was taken into account. Disks with an upper limit for the temperature were also omitted. Most of the disks in Figure 14 have temperatures falling in the range of 40–70 K (in the Solar System the Kuiper Belt exhibits similar temperature). A smaller sample shows temperatures 70 K $< T_{dust} <$ 120 K. Note that our complete sample of F-type stars contains also four disks of even higher temperature (135–200 K) published in our previous paper (Moór et al. 2009). While the age of the disk host stars belonging to the colder group ranges between 12 Myr and 3100 Myr, all warmer disks encircle stars with age <150 Myr. Using the formulae (1)–(5) in Grigorieva et al. (2007), we computed the sublimation time for possible ice grains with radii range between the blowout limit and 10 μm using the derived grain temperatures. Apart from the case of HD 24636 the timescale of sublimation is significantly longer than the age of the system. Thus, the presence of icy grains cannot be excluded in most of our disks. Note, however, that in such disks the photodesorption can remove icy mantles of grains more effectively than the sublimation (Grigorieva et al. 2007). Moreover, grains are thought to be produced in collisions that can provide enough heat to sublimate the icy mantles of the particles (Czechowski & Mann 2007). In HD 24636, the sublimation timescale is lower than the age of the system even for icy grains with a radius of a few centimeters. Taking into account the uncertainties of the timescale estimates and the derived parameters in this disk, the sublimation and the collisional timescales for the smallest grains are in the same order. If the grains are icy in this system, this finding suggests that sublimation may have a role in the removal of small grains.
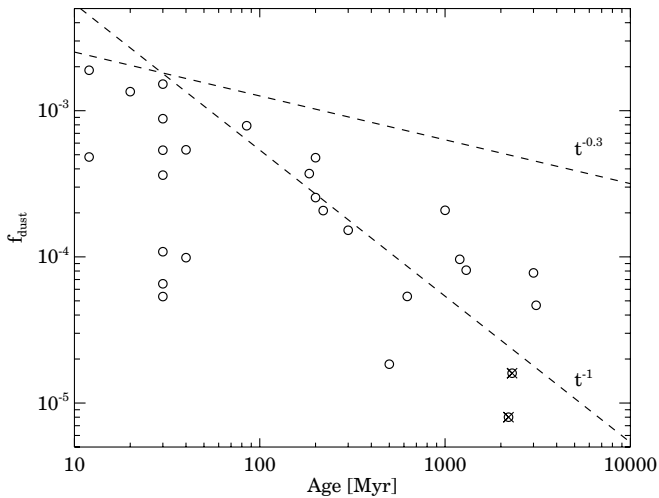
Figure 15. Fractional luminosity of the infrared excess as a function of age. Typical uncertainties in fractional luminosity range from 0.02 dex to 0.12 dex. Crosses mark disks where the excess emission was measured only in one IR band, thus they have less reliable fractional luminosities. Models of debris disk evolution predict that the decay of fractional luminosity is proportional to $t^{-\alpha}$, where α ranges between 0.3 and 1.0 (see Section 5.4). For comparison with our data, we plotted the two extremes of the evolutionary models with arbitrary normalization (dashed lines). The distribution of the data points, in particular their upper envelope, seems to suggest a decay rate halfway between the two extremes.

5.4. Fractional Luminosity

Fractional luminosity is a fundamental observable parameter of debris disks that is frequently used to characterize the amount of circumstellar matter. Figure 15 shows the derived fractional luminosities for our disks as a function of the system's age. Although the dust fractional luminosity shows a large dispersion at any given age, a clear decline with time can be recognized. Following the evolution of a narrow debris ring co-located with a planetesimal belt in an analytical steady-state collisional evolution model, Wyatt et al. (2007a) found that the fractional luminosity of the disk varies with time as $\sim t^{-1}$. In the framework of a more realistic numerical evolution model, Löhne et al. (2008) lifted some simplifications of the above-mentioned analytical model by taking into account that planetesimal strength depends on their size and the complex grain size distribution close to the blowout limit. They predicted that the decay of dust luminosity is proportional to $t^{-\alpha}$, with $\alpha = 0.3$–0.4. Kenyon & Bromley (2008) dealt with the formation and evolution of an extended planetesimal disk using a numerical model. They found that the maximum in the dust emission coincides with the formation of 1000–2000 km sized planetesimals at the inner edge of the disk. Therefore, the fractional luminosity of a disk starts to rise when large planetesimals appear at the inner edge of the disk and stir the motion of smaller bodies, initiating their destructive collisions. After the rise to a peak brightness, a slow, roughly power-law decline is predicted, $f_{\rm dust} \propto t^{-\alpha}$ with $\alpha \sim 0.6$–1.0. In Figure 15, we plotted the two extremes of these model predictions ($\alpha = 0.3$ and $\alpha = 1.0$). The distribution of the data points, in particular their upper envelope, seems to suggest a decay rate halfway between the two extremes.

The steady-state evolution model of Wyatt et al. (2007a) predicted that in the course of the evolution of a narrow debris ring, at any given age there is a maximum fractional dust luminosity ($f_{\rm max}$), since originally more massive disks eat up their mass faster. Disks with fractional luminosity of $\gg f_{\rm max}$ could be the

result of a transient event that increases the dust production for a short period (for possible transient effects see Wyatt 2008). Using their formula (Equation (20). in Wyatt et al. 2007a) and adopting their fixed model parameters (belt width: $dr/r = 0.5$, planetesimal strength: $Q_D^* = 200$ J kg^{-1}, planetesimal eccentricity: $e = 0.05$, diameter of largest planetesimal in cascade: $D_c = 2000$ km), we computed the $f_{\rm max}$ values for our debris systems. By comparing the measured fractional luminosities (see Tables 6 and 7) with the calculated maxima we conclude that all our cold disks can be consistent with a steady-state evolutionary scenario within the uncertainties of the model. In reality, transient processes might be present but their influence is undetectable with this simple comparison. Note that this model uses a pre-stirred planetesimal belt (i.e., the stirring is initiated at $t = 0$) and that in the numerical model of Löhne et al. (2008) the dust luminosity depends on the initial mass even at late evolutionary stages. Nevertheless, taking into account the delayed stirring or the dependence on initial disk mass do not affect our conclusions since both alterations would increase the $f_{\rm max}$ at a specific age.

Due to the decline in dust mass with time, high fractional luminosity debris disks are associated mainly with young stars. The rare exceptions tend to harbor very hot debris dust, in which the ejection of a small amount of transient dust can cause a significant rise in the fractional luminosities (because of the disk's proximity to the star). Moór et al. (2006) hypothesized that all stars with $f_{\rm dust} > 5 \times 10^{-4}$ are younger than 100 Myr, therefore a high $f_{\rm dust}$ values can be used as an age indicator (see also Zuckerman & Song 2004a, but with a limit of $f_{\rm dust} > 10^{-3}$). Among our new discoveries there are two debris disks with fractional luminosity exceeding the limit of $f_{\rm dust} > 5 \times 10^{-4}$, HD 3670 and HD 36968. Both objects are proposed to belong to young moving groups (age $\leqslant 30$ Myr) in agreement with the hypothesis.

5.5. Disk Radii

In the course of disk radius estimates, we assumed the dust grains to be confined to a narrow ring and that they interact with the stellar radiation as a blackbody. The resulting $R_{\rm dust}$ values correspond to minimum possible radii and possibly underestimate the "true" radii, meaning that the real size of a specific debris disk could depart significantly from the derived $R_{\rm dust}$. However, if the disks are composed of similar dust grain populations then the differences between the real dust distribution and the assumed one would shift the computed values in a similar way (Wyatt 2008), i.e., the relative radii of the disks are better constrained than the absolute values. Thus, in the following analysis we assume that the derived values can be used to study general trends in the disk radii distribution.

Destructive collisions between planetesimals can occur when the collision velocity exceeds a critical value that requires a dynamically excited (stirred) disk. In *self-stirring* models the formation of large planetesimals in collisional coagulation among smaller planetesimals naturally leads to the formation of a debris ring as well. These oligarchs can stir up the motion of the leftover smaller bodies initializing a collisional cascade. According to the models of Kenyon & Bromley (2008), the maximum of the dust production via these collisions coincides roughly with the formation of $\sim$1000 km planetesimals in the same region. Since the formation of such large bodies requires longer time at larger radial locations, the site of the dust production in an extended planetesimal disk is thought to propagate outward. Secular perturbations by giant planets—formed previously in
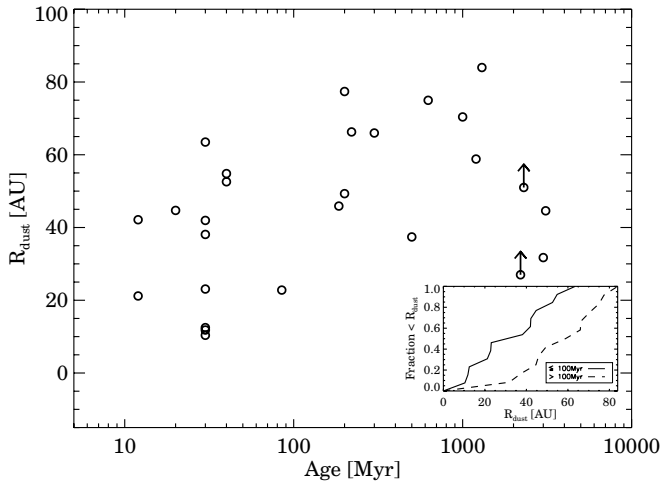
Figure 16. Derived dust radii as a function of age. Typical formal uncertainties in the derived disk radii range from 5% to 20%. The inset shows a comparison between the cumulative distribution of disks' radii around stars with age <100 Myr and stars with age >100 Myr (disks with lower limits for radius are not included). The inset does not cover any symbols.

Figure 17. Relative dust masses ($f_{dust} \cdot R_{dust}^2$, see Section 5.5) for the disks with ages of 30 Myr as a function of the derived radii.

the inner regions of the protoplanetary disk—can also initialize a collisional cascade in a planetesimal disk. Mustill & Wyatt (2009) concluded that planetary stirring can also eventuate in an outwardly propagating dust ring. In some regions the timescale of this process can be even shorter than the growth time of ~1000 km planetesimals (Mustill & Wyatt 2009). Stellar flybys can also initiate more energetic collisions in a planetesimal disk. However, such rare events are not likely to be responsible for large numbers of debris systems.

Figure 16 shows the derived radii of the dust rings as a function of age. The radii of the rings show large dispersion at any given age. The data points seem to suggest an increase of the upper envelope of the distribution with increasing age. It is even more salient that while older systems (age > 100 Myr) harbor dust rings located at radii of >30 AU, around younger systems there are several disks at radial location between 10 AU and 30 AU in a region where Saturn, Uranus, and Neptune orbit in the current configuration of our Solar System. The inset in Figure 16 shows a comparison between the cumulative distribution of disk radii around stars with age <100 Myr and stars with age >100 Myr (disks with lower limit for radius are not included). This comparison suggests a significant difference between the two distributions. Based on a Wilcoxon test, the null hypothesis that the two samples come from identical populations can be rejected on a 99.9% confidence level.

The lack of dust rings with small radii at larger ages as well as the hint for an increase of the upper envelope of the distribution are in good accordance with the predicted outward propagation of the dust production site as the result of self- or planetary stirring. Rhee et al. (2007) also reported increasing radii at larger ages for a sample of late B- and A-type stars. The latter authors estimated disk radii identically to our approach (Section 4.4), thus direct comparison with our results is meaningful. Apart from seven very extended disks (where the radius estimate was based on *IRAS* data only) the general distribution of points in Figure 7 of Rhee et al. (2007) is very similar to our results shown in Figure 16.

Kenyon & Bromley (2008) predicted that the pace of the outward propagation in a disk depends on the disk mass: the more massive the disk the faster the spread outward. Thus, during the active period of self-stirring evolution (when the
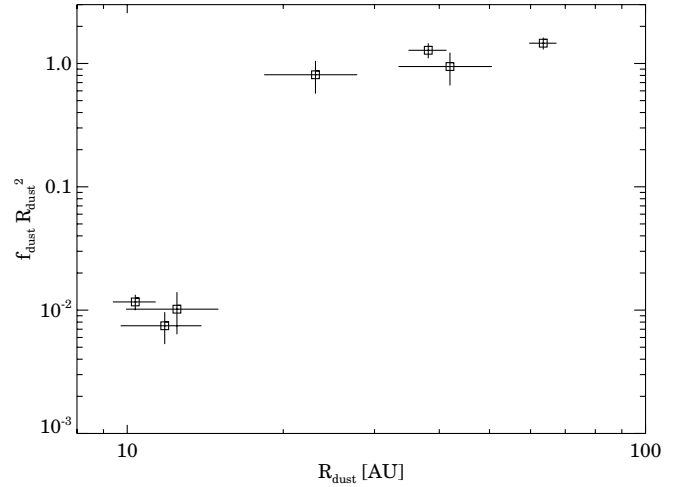
expanding ring reaches the outer boundary of the disk), in an initially more massive disk, the bright ring associated with the formation of Pluto-sized planetesimals is located at larger radius at any given age. This effect offers a good explanation for the large scatter in dust ring radii we observe for younger stars (<50 Myr). In order to test this hypothesis, we estimated the relative dust masses of the disks as $M_{dust} \propto f_{dust} R_{dust}^2$ (see Equation (7) in Wyatt 2008) for the seven 30 Myr old disks. We assume that the relative disk mass distribution does not change during disk evolution, thus the current relative masses reflect the initial mass distribution. For these disks, we displayed the relative dust masses as the function of the estimated radii of the dust ring in Figure 17. The obvious trend is fully consistent with predictions of Kenyon & Bromley (2008): more massive disks are located farther from the star.

Kenyon & Bromley (2008) derived the characteristic timescales of planetesimal disk formation and evolution processes in a disk with an initial surface density distribution of

$$\Sigma = \Sigma_0(M_*)x_m(a/a_0)^{-3/2}, \quad (5)$$

where Σ_0 is the reference surface density at a radius of a_0 = 30 AU, while x_m is a scaling factor. The reference surface density was scaled with the stellar mass as $\Sigma_0(M_*)$ = $0.18(M_*/M_\odot)$ g cm^{-2} (Σ_0 = 0.18 g cm^{-2} corresponds to the minimum mass solar nebula density at the radius of 30 AU). According to their results, the timescale for the formation of the first 1000 km icy planetesimals at a radius a can be computed as

$$t_{1000} = 145x_m^{-1.15}(a/80 \text{ AU})^3(2\ M_\odot/M_*)^{3/2}\ (\text{Myr}). \quad (6)$$

Adopting the radii of dust rings as the radii of the planetesimal belts and taking into account the derived ages of the systems, we can estimate a minimum x_m value (practically a minimum initial surface density) that is necessary for the formation of Pluto-sized planetesimals occurring at the given radial location. Assuming a fix disk geometry (R_{in} = 10 AU, R_{out} = 100 AU), an estimated initial disk mass (M_d) and an initial disk-to-star mass ratio (M_d/M_*) can also be computed (adopting the canonical gas-to-dust ratio of 100). Figure 18 shows the derived minimum $x_{m,min}$ values and the minimum initial disk-to-star mass ratios for our sample. Eight disks (HD 3670, HD 15115, HD 16743, HD 30447, HD 36968, HD 113337, HD 170773,
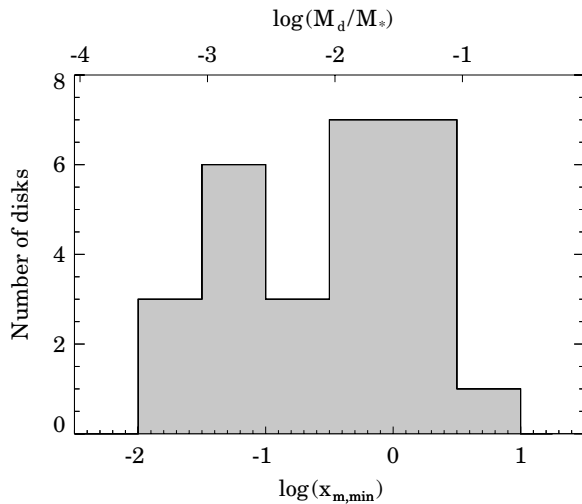
Figure 18. Histogram of the minimum $x_{m,min}$ values that are required for the observed disk to become self-stirred in $t < t_{system}$. Initial disk-to-star mass ratios corresponding to the computed $x_{m,min}$ are indicated on the top of the graph (Section 5.5).

and HD 192758) require an initial surface density higher than that of the minimum solar mass nebula. The largest $x_{m,min}$ value (3.3) was obtained for HD 16743. Assuming that self-stirring occurred in these systems and comparing the derived M_d/M_* ratios with the cumulative distribution of the corresponding ratios for protoplanetary disks in the Taurus and Ophiucus star-forming regions (Figure 7; Andrews & Williams 2007), we concluded that these eight disks might represent the high end of the disk mass distribution. Mustill & Wyatt (2009) argued that a disk with $x_{m,min} \geqslant 10$ is unlikely to be the site of a collisional cascade ignited by self-stirring. Since the highest $x_{m,min}$ in our sample is 3.3, all our disks could be the result of self-stirring. Note, however, that in the calculation of dust ring radii we assumed the presence of large blackbody grains. The presence of smaller grains that are ineffective emitters would have resulted in larger radial locations. Due to the strong dependence of the minimum initial surface density on the radial location, the uncertainty of R_{dust} can affect (usually increase) the value of $x_{m,min}$.

Six out of the eight disks where our calculations implied high initial surface density are younger than 60 Myr (see Table 8) and are located within 80 pc (Table 1). These systems might be good targets for future planet searching surveys via direct imaging, because (1) according to the models, disks with high initial surface density are favorable for planet formation and (2) young ages make giant planets more easily detectable (since they are still bright). We note that HR 8799, Fomalhaut, and β Pic, systems hosting massive outer planets, harbor massive bright debris disks as well.

In the present Solar System, planetesimals reside mainly in two spatially separated belts, the Kuiper Belt and the main asteroid belt. Infrared and submillimeter observations of debris disks implied that stars harboring multiple component disks might be common (Chen et al. 2009; Smith & Wyatt 2010, and references therein). The dust replenishment processes may also be similar to those in our Solar System: collisions between planetesimals are thought to lead to the production of fresh dust in the outer cold rings, while besides the collisions, sublimation of icy planetesimals (scattered from the outer reservoir) can also contribute to the maintenance of the inner warm dust belt. Several of these systems are younger than 100 Myr

and their age coincides well with the era of terrestrial planet formation in our Solar System (see Apai & Lauretta 2010, for a review), a process believed to be accompanied with the release of a huge amount of dust grains due to collisions between large protoplanets (Kenyon & Bromley 2004b). The warm dust around these young stars might either originate from terrestrial planet formation (e.g., Lisse et al. 2008) or from the collisional grinding of a rocky asteroidal belt. In Section 4.4, we found five debris systems where the SED can be fitted better with a two-component temperature model than with a single temperature one. Assuming that the warm component is associated with inner dust rings we propose that these five stars harbor two spatially separated dust rings co-located with two distinct planetesimal belts. All of these systems are younger than 40 Myr. Taking into account the above-mentioned arguments, these five warm dust rings might also be linked to the formation of terrestrial planets or collisional evolution of an asteroid belt. Since the characteristic temperature of the dust grains (150–180 K) significantly exceeds the sublimation temperature of comets (~110 K; Wyatt 2008), cometary activity can also play a role in the replenishment of warm dust particles. Moór et al. (2009) found two young F-type members of the Tucana-Horologium association (HD 13246 and HD 53842) that harbor warm debris rings with properties ($T_{dust} \sim 150$–170 K, $f_{dust} \sim (0.5$–$1.7) \times 10^{-4}$) very similar to those of the currently analyzed five disks. The inner zone of the two Tucana-Horologium stars might also be sites of intense planet formation, although, no cold excess emission has been seen toward them. The lack of observable cold excess may suggest a relatively dust-free outer disk perhaps caused by disk truncation.

6. SUMMARY

With the aim of investigating the properties and evolutionary trends of debris disks around F-type stars, we observed 82 targets with the *Spitzer Space Telescope* using the IRS and MIPS instruments to obtain infrared spectroscopy and photometry. The core sample was selected based on hints for excess emission in earlier infrared observations, and this sample was supplemented by F-type members of some young kinematic groups. We found 27 stars that harbor debris disks, 9 of which are new discoveries. Apart from two stars, all of the observed disks exhibit excess in the IRS spectra, and 17 disks were detected even at 160 μm. In two cases, the emission was found to be marginally extended on the 70 μm MIPS images. Combining the MIPS and IRS measurements with additional data taken from former infrared space missions (*IRAS*, *ISO*) and ground-based submillimeter/millimeter (SCUBA, IRAM) observations, we compiled the SED of the targets. Thanks to the large number of measurements at different wavelengths we achieved excellent spectral coverage for most of our debris systems. We have modeled the excess emission of 22 debris disks using a single temperature dust ring model and 5 debris systems with a two-temperature model. The latter systems may contain two dust rings around the star. All of our disks were found to be collision dominated.

Among the 27 disks, 15 encircle stars that likely belong to young moving groups, offering accurate age estimates for these systems. We identified five new moving group members. HD 15745, that exhibit one of the largest fractional luminosities among northern debris disks, is a likely member of the β Pic moving group. HD 36968, a system with high fractional luminosity, can be assigned to the recently discovered Octans kinematic group (Torres et al. 2008), being the first member where the existence of a debris disk was discovered.

In accordance with the expected trends, the fractional luminosity of the disks declines with time. The distribution of data points, in particular their upper envelope, seems to suggest a decay rate falling within the range of the model predictions ($f_{dust} \propto t^{-0.3}$–$t^{-1.0}$; Dominik & Decin 2003; Wyatt et al. 2007a; Löhne et al. 2008; Kenyon & Bromley 2008). All disks in the sample seem to be consistent with quasi-steady-state evolutionary scenarios of Wyatt et al. (2007a).

Assuming blackbody grains, we computed the radial location of the cold dust rings in all debris systems. We found a hint for an increase of the upper envelope of the radius distribution with increasing age. While older systems (age > 100 Myr) harbor dust rings located at radii of >30 AU, around younger systems there are several disks at radial location between 10 and 30 AU. Both findings are in accordance with the predictions of self- or planetary-stirring theories of Kenyon & Bromley (2008) and Mustill & Wyatt (2009).

Facilities: Spitzer (), *ISO* (), *IRAS* (), IRAM:30m ()

REFERENCES

Andrews, S. M., & Williams, J. P. 2007, ApJ, 671, 1800
Apai, D. A., & Lauretta, D. S. 2010, Protoplanetary Dust: Astrophysical and Cosmochemical Perspectives (Cambridge: Cambridge Univ. Press)
Asiain, R., Figueras, F., Torra, J., & Chen, B. 1999, A&A, 341, 427
Backman, D. E., & Paresce, F. 1993, in Protostars and Planets III, ed. E. H. Levy & J. I. Lunine (Tucson, AZ: Univ. Arizona Press), 1253
Balachandran, S. 1990, ApJ, 354, 310
Balega, I. I., Balega, Y. Y., Maksimov, A. F., Malogolovets, E. V., Rastegaev, D. A., Shkhagosheva, Z. U., & Weigelt, G. 2007, Astrophys. Bull., 62, 339
Balog, Z., Kiss, L. L., Vinkó, J., Rieke, G. H., Muzerolle, J., Gáspár, A., Young, E. T., & Gorlova, N. 2009, ApJ, 698, 1989
Batten, A. H., & Morbey, C. L. 1980, PASP, 92, 98
Beichman, C. A., et al. 2006, ApJ, 652, 1674
Berthet, S. 1990, A&A, 227, 156
Boesgaard, A. M. 1987, ApJ, 321, 967
Boesgaard, A. M., Armengaud, E., King, J. R., Deliyannis, C. P., & Stephens, A. 2004, ApJ, 613, 1202

Boesgaard, A. M., Budge, K. G., & Burck, E. E. 1988a, ApJ, 325, 749
Boesgaard, A. M., Budge, K. G., & Ramsay, M. E. 1988b, ApJ, 327, 389
Boesgaard, A. M., & Friel, E. D. 1990, ApJ, 351, 467
Boesgaard, A. M., & Tripicco, M. J. 1986, ApJ, 303, 724
Bouwman, J., et al. 2008, ApJ, 683, 479
Bryden, G., Tanner, A., Beichman, C., Stapelfeldt, K., Rieke, G., & Wyatt, M. 2006, BASS, 38, 583
Buchanan, C. L., Gallimore, J. F., O'Dea, C. P., Baum, S. A., Axon, D. J., Robinson, A., Elitzur, M., & Elvis, M. 2006, AJ, 132, 401
Carpenter, J. M., Mamajek, E. E., Hillenbrand, L. A., & Meyer, M. R. 2009a, ApJ, 705, 1646
Carpenter, J. M., et al. 2008, ApJS, 179, 423
Carpenter, J. M., et al. 2009b, ApJS, 181, 197
Castelli, F., & Kurucz, R. L. 2003, in IAU Symp. 210, Modelling of Stellar Atmospheres, ed. N. E. Piskunov, W. W. Weiss, & D. F. Gray (San Francisco, CA: ASP), A20
Cenarro, A. J., et al. 2007, MNRAS, 374, 664
Chen, C. H., Sheehan, P., Watson, D. M., Manoj, P., & Najita, J. R. 2009, ApJ, 701, 1367
Chen, C. H., et al. 2006, ApJS, 166, 351
Currie, T., Kenyon, S. J., Balog, Z., Rieke, G., Bragg, A., & Bromley, B. 2008, ApJ, 672, 558
Czechowski, A., & Mann, I. 2007, ApJ, 660, 1541
da Silva, L., Torres, C. A. O., de La Reza, R., Quast, G. R., Melo, C. H. F., & Sterzik, M. F. 2009, A&A, 508, 833
Debes, J. H., Weinberger, A. J., & Song, I. 2008, ApJ, 684, L41
Decin, G., Dominik, C., Waters, L. B. F. M., & Waelkens, C. 2003, ApJ, 598, 636
Dominik, C., & Decin, G. 2003, ApJ, 598, 626
Dommanget, J., & Nys, O. 2002, Observations et Travaux, 54, 5
Edvardsson, B., Andersen, J., Gustafsson, B., Lambert, D. L., Nissen, P. E., & Tomkin, J. 1993, A&A, 275, 101
Eggen, O. J. 1982, ApJS, 50, 221
Engelbracht, C. W., et al. 2007, PASP, 119, 994
ESA 1997, The Hipparcos and Tycho Catalogues (ESA SP-1200; Noordwijk: ESA)
Forbrich, J., Lada, C. J., Muench, A. A., & Teixeira, P. S. 2008, ApJ, 687, 1107
Frankowski, A., Jancart, S., & Jorissen, A. 2007, A&A, 464, 377
Friel, E. D., & Boesgaard, A. M. 1992, ApJ, 387, 170
Gáspár, A., Rieke, G. H., Su, K. Y. L., Balog, Z., Trilling, D., Muzzerole, J., Apai, D., & Kelly, B. C. 2009, ApJ, 697, 1578
Gautier, T. N., III, et al. 2007, ApJ, 667, 527
Gordon, K. D., et al. 2007, PASP, 119, 1019
Gorlova, N., Rieke, G. H., Muzerolle, J., Stauffer, J. R., Siegler, N., Young, E. T., & Stansberry, J. H. 2006, ApJ, 649, 1028
Gray, R. O., & Corbally, C. J. (ed.) 2009, Stellar Spectral Classification (Princeton, NJ: Princeton Univ. Press)
Gray, R. O., Corbally, C. J., Garrison, R. F., McFadden, M. T., Bubar, E. J., McGahee, C. E., O'Donoghue, A. A., & Knox, E. R. 2006, AJ, 132, 161
Gray, R. O., Corbally, C. J., Garrison, R. F., McFadden, M. T., & Robinson, P. E. 2003, AJ, 126, 2048
Greaves, J. S., Fischer, D. A., & Wyatt, M. C. 2006, MNRAS, 366, 283
Grigorieva, A., Thébault, P., Artymowicz, P., & Brandeker, A. 2007, A&A, 475, 755
Guillout, P., et al. 2009, A&A, 504, 829
Hauck, B., & Mermilliod, M. 1997, VizieR Online Data Catalog, 2215, 0
Higdon, S. J. U., et al. 2004, PASP, 116, 975
Hillenbrand, L. A., et al. 2008, ApJ, 677, 630
Holmberg, J., Nordström, B., & Andersen, J. 2007, A&A, 475, 519
Holmberg, J., Nordström, B., & Andersen, J. 2009, A&A, 501, 941
Houck, J. R., et al. 2004, ApJS, 154, 18
Kalas, P., Duchene, G., Fitzgerald, M. P., & Graham, J. R. 2007a, ApJ, 671, L161
Kalas, P., Fitzgerald, M. P., & Graham, J. R. 2007b, ApJ, 661, L85
Kalas, P., Graham, J. R., Beckwith, S. V. W., Jewitt, D. C., & Lloyd, J. P. 2002, ApJ, 567, 999
Kennedy, G. M., & Wyatt, M. C. 2010, MNRAS, 405, 1253
Kenyon, S. J., & Bromley, B. C. 2004a, AJ, 127, 513
Kenyon, S. J., & Bromley, B. C. 2004b, ApJ, 602, L133
Kenyon, S. J., & Bromley, B. C. 2008, ApJS, 179, 451
King, J. R., & Schuler, S. C. 2005, PASP, 117, 911
King, J. R., Villarreal, A. R., Soderblom, D. R., Gulliver, A. F., & Adelman, S. J. 2003, AJ, 125, 1980
Kleinmann, S. G., Cutri, R. M., Young, E. T., Low, F. J., & Gillett, F. C. 1986, Explanatory Supplement to the IRAS Serendipitous Survey Catalog (Pasadena, CA: JPL)

Krist, J. 2002, Tiny Tim/SIRTF User's Guide, Technical Report (Pasadena, CA: SSC)

Lallement, R., Welsh, B. Y., Vergely, J. L., Crifo, F., & Sfeir, D. 2003, A&A, 411, 447

Lawler, S. M., et al. 2009, ApJ, 705, 89

Lisse, C. M., Chen, C. H., Wyatt, M. C., & Morlok, A. 2008, ApJ, 673, 1106

Löhne, T., Krivov, A. V., & Rodmann, J. 2008, ApJ, 673, 1123

Lu, N., et al. 2008, PASP, 120, 328

Luhman, K. L., Stauffer, J. R., & Mamajek, E. E. 2005, ApJ, 628, L69

Makovoz, D., & Marleau, F. R. 2005, PASP, 117, 1113

Mamajek, E. E., & Hillenbrand, L. A. 2008, ApJ, 687, 1264

Mannings, V., & Barlow, M. J. 1998, ApJ, 497, 330

McQuarrie, A. D. R., & Tsai, C. 1998, Regression and Time Series Model Selection (Singapore: World Scientific), 32

Mentuch, E., Brandeker, A., van Kerkwijk, M. H., Jayawardhana, R., & Hauschildt, P. H. 2008, ApJ, 689, 1127

Meyer, M. R., et al. 2006, PASP, 118, 1690

Meyer, M. R., et al. 2008, ApJ, 673, L181

Monier, R. 2005, A&A, 442, 563

Moór, A., Ábrahám, P., Derekas, A., Kiss, C., Kiss, L. L., Apai, D., Grady, C., & Henning, T. 2006, ApJ, 644, 525

Moór, A., et al. 2009, ApJ, 700, L25

Morales, F. Y., et al. 2009, ApJ, 699, 1067

Moshir, M., et al. 1989, Explanatory Supplement to the IRAS Faint Source Survey (Pasadena, CA: JPL) (FSC)

Munari, U., Sordo, R., Castelli, F., & Zwitter, T. 2005, A&A, 442, 1127

Mustill, A. J., & Wyatt, M. C. 2009, MNRAS, 399, 1403

Najita, J., & Williams, J. P. 2005, ApJ, 635, 625

Nilsson, R., et al. 2010, A&A, 518, A40

Perryman, M. A. C., et al. 1998, A&A, 331, 81

Pourbaix, D. 2000, A&AS, 145, 215

Rebull, L. M., et al. 2008, ApJ, 681, 1484

Reddy, B. E., Tomkin, J., Lambert, D. L., & Allende Prieto, C. 2003, MNRAS, 340, 304

Reid, I. N., Cruz, K. L., & Allen, P. R. 2007, AJ, 133, 2825

Rhee, J. H., Song, I., Zuckerman, B., & McElwain, M. 2007, ApJ, 660, 1556

Rieke, G. H., et al. 2004, ApJS, 154, 25

Rieke, G. H., et al. 2005, ApJ, 620, 1010

Saffe, C., Gómez, M., Pintado, O., & González, E. 2008, A&A, 490, 297

Saxton, R. D., Read, A. M., Esquej, P., Freyberg, M. J., Altieri, B., & Bermejo, D. 2008, A&A, 480, 611

Schneider, G., et al. 2006, ApJ, 650, 414

Sestito, P., & Randich, S. 2005, A&A, 442, 615

Siegler, N., Muzerolle, J., Young, E. T., Rieke, G. H., Mamajek, E. E., Trilling, D. E., Gorlova, N., & Su, K. Y. L. 2007, ApJ, 654, 580

Siess, L., Dufour, E., & Forestini, M. 2000, A&A, 358, 593

Smith, R., & Wyatt, M. C. 2010, A&A, 515, A95

Spangler, C., Sargent, A. I., Silverstone, M. D., Becklin, E. E., & Zuckerman, B. 2001, ApJ, 555, 932

Stansberry, J. A., et al. 2007, PASP, 119, 1038

Su, K. Y. L., et al. 2005, ApJ, 628, 487

Su, K. Y. L., et al. 2006, ApJ, 653, 675

Su, K. Y. L., et al. 2009, ApJ, 705, 314

Takeda, Y. 2007, PASJ, 59, 335

Tanner, A., Beichman, C., Bryden, G., Lisse, C., & Lawler, S. 2009, ApJ, 704, 109

Thébault, P., & Augereau, J.-C. 2007, A&A, 472, 169

Torres, C. A. O., Quast, G. R., Melo, C. H. F., & Sterzik, M. F. 2008, in Handbook of Star Forming Regions, Volume II, The Southern Sky, ed. B. Reipurth (San Francisco, CA: ASP), 757

Trilling, D. E., et al. 2007, ApJ, 658, 1289

Trilling, D. E., et al. 2008, ApJ, 674, 1086

Valenti, J. A., & Fischer, D. A. 2005, ApJS, 159, 141

van Leeuwen, F. (ed.) 2007, Hipparcos, the New Reduction of the Raw Data (Astrophysics and Space Science Library 350; Dordrecht: Springer)

Werner, M. W., et al. 2004, ApJS, 154, 1

West, A. A., Hawley, S. L., Bochanski, J. J., Covey, K. R., Reid, I. N., Dhital, S., Hilton, E. J., & Masuda, M. 2008, AJ, 135, 785

Williams, J. P., & Andrews, S. M. 2006, ApJ, 653, 1480

Wright, C. O., Egan, M. P., Kraemer, K. E., & Price, S. D. 2003, AJ, 125, 359

Wright, J. T., Marcy, G. W., Butler, R. P., & Vogt, S. S. 2004, ApJS, 152, 261

Wu, Y., Charmandaris, V., Huang, J., Spinoglio, L., & Tommasin, S. 2009, ApJ, 701, 658

Wyatt, M. C. 2005, A&A, 433, 1007

Wyatt, M. C. 2006, ApJ, 639, 1153

Wyatt, M. C., Smith, R., Greaves, J. S., Beichman, C. A., Bryden, G., & Lisse, C. M. 2007a, ApJ, 658, 569

Wyatt, M. C., Smith, R., Su, K. Y. L., Rieke, G. H., Greaves, J. S., Beichman, C. A., & Bryden, G. 2007b, ApJ, 663, 365

Wyatt, M. C. 2008, ARA&A, 46, 339

Young, E. T., et al. 2004, ApJS, 154, 428

Zuckerman, B., & Song, I. 2004a, ApJ, 603, 738

Zuckerman, B., & Song, I. 2004b, ARA&A, 42, 685